Fall 2019

A Spatial Heterodyne Spectrometer for Raman Imaging and Remote Spectroscopy

Ashley Nicole Allen

A SPATIAL HETERODYNE SPECTROMETER FOR RAMAN IMAGING AND REMOTE SPECTROSCOPY

by

Ashley Nicole Allen

Bachelor of Science
Charleston Southern University, 2015

Submitted in Partial Fulfillment of the Requirements

For the Degree of Doctor of Philosophy in

Chemistry

College of Arts and Sciences

University of South Carolina

2019

Accepted by:

S. Michael Angel, Major Professor

John L. Ferry, Chair, Examining Committee

Hui Wang, Committee Member

Alan W. Decho, Committee Member

Cheryl L. Addy, Vice Provost and Dean of the Graduate School

DEDICATION

I dedicate this work to my father, Walter Preston Allen, my number one fan and greatest inspiration.

ACKNOWLEDGEMENTS

First, I express my utmost gratitude to my research advisor, Dr. S. Michael Angel, for his exceptional patience, encouragement and for providing me with every opportunity possible to advance my career. I'd like to thank Dr. J. Chance Carter for his constant support and research collaboration.

I thank my committee members, Dr. John L. Ferry, Dr. Hui Wang, and Dr. Alan W. Decho for their helpful advice and service on my committee. I also appreciate the professors at Charleston Southern University, especially Dr. Stephen D. Hudson, Dr. Xiangdong Bi, and Dr. Jamie Probin for preparing me for graduate education.

Thank you to my current and former lab mates and colleagues: Nirmal Lamsal, Joseph Bonvallet, K. Alicia Strange-Fessler, Patrick Barnett, Josh Huntington, Izlen Peksenar, Abigail Waldron, Arelis Colon, Joshua Ottoway, Mike Ritter, Sam Putnam and Hannah Liberatore for your support and guidance throughout the years.

I honor the Allen family for their lifelong support of my education. A special thanks to Donna Allen, Kathy Oddo, Mary Chilton and Mary Riley.

ABSTRACT

Raman and Laser-Induced Breakdown Spectroscopy (LIBS) are optical techniques that provide information about the chemical makeup of a sample without any preparation or physical contact with it. For this reason, Raman and LIBS spectrometers are among the instruments selected for NASA's Mars 2020 rover mission and are being considered for future missions to the Jovian moons, asteroids and comets. Such future missions will require smaller, more ruggedized Raman and LIBS spectrometers, and the new type of spectrometers discussed here, the spatial heterodyne Raman and LIBS spectrometers are being developed for this purpose. The SHS is a wide-field, Fourier transform, stationary grating interferometer with no moving parts, that is well-suited for miniature Raman and LIBS spectrometers. The spectral resolution of the SHS is not strongly dependent upon entrance aperture size, so the footprint can be very small while still allowing for high resolution spectral measurements. The SHS has a large entrance aperture and a wide acceptance angle that provides much higher light throughput than a dispersive slit-based spectrometer of comparable resolution. Lastly, because the SHS has no moving parts and the spectral resolution is not strongly tied to its size, it can be built monolithically making it both small and robust.

This thesis explores alternative optical configurations of the SHS collection optics that are useful for miniaturizing or extending the capabilities of a remote SHS Raman or LIBS system. A lightweight, low cost Fresnel lens was compared to that of a high-quality telescope for standoff signal collection. This takes advantage of the wide field of view of

the SHS, which makes the collection efficiency very forgiving of the quality of the collection optics. We observed that the signal collected by the Fresnel lens, which weighed less than 1% of a comparable glass lens, was only about four times less than that of the telescope. This suggests that Fresnel optics would be useful in applications where size and weight are restricted, such as in instruments designed for spacecraft and planetary landers.

In other studies, a new hyperspectral Raman imaging technique is demonstrated using a spatial heterodyne Raman spectrometer with a microlens array, where the entire hypercube of spatial and spectral information is obtained in a single measurement. Raman images for a variety of sample types are demonstrated where complete Raman spectra, at spectral ranges from 1200 cm^{-1} to 2800 cm^{-1}, were acquired independently at each spatial point, for 60 to >500 unique spatial points, in a single spectral acquisition. The spectral resolution of the Raman spectra acquired for each spatial point in the images varied from 32 cm^{-1} to 148 cm^{-1}, dependent on the grating and system magnification and the resolution of the detector. Calculations show that this technique can be extended to include more than 10,000 spatial points with a spectral resolution of 20 cm^{-1}, over a large spectral range.

TABLE OF CONTENTS

LIST OF FIGURES

CHAPTER 1

REMOTE SPECTROSCOPY AND RAMAN CHEMICAL IMAGING

1.1 REMOTE SPECTROSCOPY FOR PLANETARY EXPLORATION

Are we alone in the universe? Answering this question is a priority to space agencies around the world. Rugged, self-sufficient instruments for remote chemical identification are needed to help answer questions regarding planetary geology and surface chemistry that might give insight into past and present life on other planets. The National Research Council Visions and Voyages for Planetary Science in the Decade 2013-2022 recommends a high priority be placed on remote sensing technology with a focus on developing and maturing novel, crosscutting, low mass/power sensors integrated into robust, low-cost system architectures.[1] The Decadal survey also lists ultraviolet/visible/infrared/Raman spectroscopes as one of the most commonly cited improvements required in instrumentation for future planned NASA missions (Table 10.2 on page 291 of ref. 1).[1] Improvements are needed in the four following areas: (1) Increased Resolution, (2) Reduction of Mass, (3) Radiation Resistance and (4) Ability to Operate in Extreme environments. This thesis is focused on developing instrumentation for two different optical techniques, laser-induced breakdown spectroscopy (LIBS) and Raman spectroscopy, with a focus on addressing the needs outlined in the Decadal Survey.

1.2 LASER-INDUCED BREAKDOWN SPECTROSCOPY (LIBS)

Laser-induced breakdown spectroscopy (LIBS) is an active remote sensing technique that measures atomic emission. LIBS is a well-developed technique used in applications including food, archaeology, engineering, metallurgy and deep ocean analysis. There are numerous articles, reviews and textbooks that describe LIBS in depth, so only a brief summary is given here.[2-6] Section 1.5 summarizes LIBS instrumentation.

A high power, pulsed laser is focused on the sample to ablate and atomize the material,

forming a plasma. The hot plasma excites the ablated atoms which emit photons at characteristic wavelengths. The light is collected and analyzed with an emission spectrometer equipped with a gated detector and analyzed to reveal the chemical makeup of the sample. LIBS requires no sample preparation and is well suited for remote and in-situ analysis. A gated detector is used in LIBS to gate out the continuum emission of the plasma itself, which is the main background noise contributor in LIBS, and the gate width and gate delay of the detector are optimized to isolate the LIBS emission as the plasma cools. The emission intensity is related to the concentration of the emitting element, but calibration is required for quantitative measurements. The measurement time depends on the number of shots required. LIBS measurements can be made remotely and require no physical contact with the sample. LIBS is minimally destructive to the sample, and repetitive ablation can actually be advantageous to remove dust and weathered surface layers for planetary measurements. LIBS is a sensitive technique and can determine elements of high and low atomic numbers with limits of detection in the range 1-1000 ppm (wt/wt).[7] It is for these reasons that LIBS is an important part of planetary science payloads.

The first LIBS measurements in space were performed using the ChemCam instrument on NASA's Mars Science Laboratory Rover *Curiosity* beginning August of 2012. To date, over 500,000 laser shots have been measured on the surface of Mars using the ChemCam. The instrument also provides context imaging.[8-9] An improved version of ChemCam, called SuperCam, is included on the upcoming Mars 2020 mission. In addition to LIBS and context imaging, SuperCam will also measure Raman spectroscopy; a first for this type of spectroscopy.[10]

1.3 RAMAN SPECTROSCOPY

Raman spectroscopy has numerous applications outlined in a recent review that include identifying minerals, ices, and organic molecules that may indicate past or extant life.[11] Two Raman spectrometers are planned for the upcoming NASA Mars 2020 mission and a Raman instrument is planned for Europe's ExoMars mission, also scheduled in 2020. The Mars rovers are relatively large, the planetary conditions relatively benign, and the planned Raman instruments are of relatively conventional design. Other missions such as planned missions to Europa, or missions to any of the outer moons, planets, or comets will require much smaller instruments with a greater range of capabilities and resistance to harsh conditions such as low temperatures and high amounts of radiation. Commercial Raman systems are not suitable for the rigors of such space applications.

Raman is a vibrational spectroscopy that can be used to analyze solid, liquid, or gaseous samples without any sample preparation. Unlike IR spectroscopy, Raman is well suited for measuring aqueous solutions because the Raman cross section for water is low and water is transparent at wavelengths that are typically used for Raman. Raman scattering is an inelastic light scattering process that happens when the molecule undergoes a polarizability change causing it to gain or lose a quantum of vibrational energy through a virtual state. As shown in the energy level diagram in figure 1.1, energy gain is known as anti-Stokes while energy loss is referred to as Stokes scattering. However, most molecular scattered light is elastically scattered, known as Rayleigh scattering, with no change of wavelength. In Raman spectroscopy, the intensity, energy, bandwidth and band shape of the scattered light can be used to determine chemical identity and chemical state.[12] The intensity of Raman scattered light, I_R, is given by Eq. 1.1:[13]

$$I_R = D(\nu_{ex}^4)\, E_0\, n_i\, e^{(\Delta E_i/kT)} \qquad \text{Eq. 1.1}$$

Where $D(\nu_{ex}^4)$ is the frequency dependent Raman cross-section, ν_{ex} is the excitation frequency, E_0 is the incident power, n_i is the number density in state i, and the exponential is the Boltzmann factor for state i. At room temperature, Stokes shifted Raman is generally more intense than anti-Stokes because it arises from the vibrational ground state while anti-stokes originates from a higher vibrational state. The limitations of Raman spectroscopy arise from the fact that Raman scatter is a low probability event that competes with more quantum-mechanically favored absorption/emission processes such as fluorescence. Even so, choosing the appropriate wavelength or time-gating can help minimize fluorescence. The detected Raman signal, S, dependence on instrumental parameters is given by Eq. 1.2:

$$S = I_R\, K\, A\, \Omega\, T\, Q\, t \qquad \text{Eq. 1.2}$$

where K is the sample path length, A is the sample area viewed, Ω is the collection solid angle, T is the transmission of the measurement system, Q is the quantum efficiency of the detector and t is the measurement time. A typical Raman cross section is on the order of 10^{-30} – 10^{-34} cm^2 $molecule^{-1}$ sr^{-1}. Every component of a Raman spectroscopic system is designed to produce and isolate the maximum Raman signal.

1.4 RAMAN INSTRUMENTATION

Raman systems consist of a source, illumination, collection and filtering optics, a spectrometer, and a detector; with each component optimized for the application. Standoff or remote Raman implies sample illumination and signal collection for a sample located a few to many tens of meters distance. Raman and LIBS systems share many of the same components and a single spectrometer can be used to make both measurements. A description of LIBS instrumentation is given in section 1.5.

1.4.1 EXCITATION SOURCE

The Raman excitation source should be intense and monochromatic. The width of a Raman band is related to its natural linewidth, bandwidth of the excitation source and the spectral resolving power of the spectrometer used. Raman scatter appears as a shift from the laser line, so Raman bands excited via broadband illumination source will have larger full-width half-maximum spectral resolution than that of a narrow band illumination source. The most commonly used source for Raman measurements is a laser due to its narrow linewidths and high source powers. More efficient light emitting diodes (LEDs) are beginning to surface as viable Raman sources, however these sources are still subject to limitations.[14]

While any wavelength can be used to obtain a Raman spectrum, shorter excitation wavelengths can provide larger sensitivity because the Raman scattering cross-section is proportional to the fourth power of the frequency of the Raman transition. However, one should also take processes that compete with Raman scattering into account when considering source wavelength. Longer wavelengths like 785 nm and 1064 nm are commonly used to avoid exciting fluorescence, but Raman signals excited with these wavelengths are weaker than those excited with visible radiation because of the frequency dependence of the Raman cross-section. Alternatively, deep-ultraviolet wavelengths can be used to excite the sample and avoid fluorescence.

The Raman excitation source can be continuous or pulsed, but care must be taken to ensure photodegradation of samples does not occur. The use of a pulsed laser with a gated detector allows one to make measurements in daylight conditions because persistent stray light and long-lived fluorescence are gated out. A narrow bandpass filter or laser-line

dichroic mirror is used between the sample and source to remove background spontaneous emission from the laser.

1.4.2 FILTERING AND COLLECTION OPTICS

Generally, for Raman the incident light is focused as tightly as possible on the sample so that the maximum Raman signal can be collected and focused into the entrance slit of a spectrometer. In some cases, the incident beam is expanded to prevent photodegradation of samples. Illumination and collection are typically done on different optical axes in order to maximize collection solid angle and to block stray source light, but coaxial illumination/collection is also used. The collection optic serves to send Raman light into the spectrometer. Since Raman scattering is very weak compared to Rayleigh, a laser blocking notch filter is required to filter out the intense source and Rayleigh scattered signal.

1.4.3 SPECTROMETERS

For Raman, either a spectrometer or an interferometer is used as the wavelength selector. The most common commercial Raman systems use a dispersive, slit-based spectrometer to directly separate wavelengths of the Raman spectrum with a resolution that is dependent on the entrance slit width, line density and size of the gratings. In a dispersive spectrometer, increasing resolution sacrifices light throughput and thus sensitivity. Commercial Fourier transform (FT) Raman systems use a Michelson interferometer with moving mirrors that are scanned to obtain an interferogram. All source wavelengths are measured simultaneously in an interferometer and higher light throughput can be achieved than that of a dispersive slit-based system of comparable resolving power. The disadvantages of interferometers are discussed in chapter 2. The resolving power of the

Michelson interferometer depends on the magnitude of the mirror's displacement. Regardless of the spectrometer, a photodetector is used to capture the Raman signal and a computer is used to process it.

1.4.4 DETECTORS

A charge coupled device (CCD) or a complementary metal oxide semiconductor (CMOS) are two different technologies for capturing digital images. CCD based imagers have been preferred for Raman because they achieve a higher fill-factor and have very low noise. However, recent improvements in CMOS detector technology have made them comparable to or even better than CCDs in both respects. There are technical tradeoffs between the two, and the choice now depends on the application. For a CCD, all pixels are read out through a limited number of nodes and "read" off the chip as an analog signal. CCDs are shot noise limited but they require cooling, thermoelectrically or by liquid nitrogen, to reduce the thermal noise. In contrast, every pixel of a CMOS sensor has its own charge to voltage conversion and the chip outputs a digital signal. This allows for high speed readout but increases design complexity and reduces the pixel's active area. CMOS detectors offer the advantage of significantly lower power consumption, fast readout, higher pixel density and the ability to do on-chip signal integration. High speed CMOS detectors have lower noise than high speed CCDs. To sum multiple accumulations, CCDs combine signal charges while CMOS combine voltage signals. This is noiseless for CCDs but not for CMOS, so CCDs are preferred for weak signals requiring long accumulations.[15,16]

1.5 LIBS INSTRUMENTATION

LIBS and Raman instruments share many common components but have a few

important differences. In LIBS, the laser must be pulsed and focused onto the sample to create a plasma. Like Raman, any laser wavelength can, in principle, be used for LIBS, but there are wavelength effects that are detailed in references 4 and 5.[4,5] It is possible to measure both Raman and LIBS with the same instrument provided it uses a pulsed laser/gated detector and there is a method of controlling the laser fluence on the sample, such as focusing and defocusing the laser beam on the sample. A gated detector is required to separate atomic emission from the high intensity Bremsstrahlung radiation that occurs in the beginning of the LIBS plasma. The timing parameters, gate delay and gate width, are optimized to capture the LIBS emission after the laser fires. For Raman, the detector is gated on only during the laser pulse.

1.6 RAMAN CHEMICAL IMAGING

Raman imaging is useful for measuring heterogeneous samples. Chapter 4 of this thesis describes an innovative way to perform two-dimensional (2D) Raman chemical imaging, so we must discuss Raman imaging in general.

A Raman image is an array of spatially accurate Raman spectra. Traditional, non-imaging Raman provides a mean spectrum that represents the bulk composition of the material measured. However, real-world samples are generally heterogeneous, so this mean spectrum can be vastly different than the localized spectra at different points on the sample. In order to fully characterize heterogeneous materials, there is a need to measure chemical properties in multiple spatial dimensions.[17]

1.6.1 SCANNING METHODS

The first Raman imaging microprobes, developed in the 1970's, have used mostly scanning-based instrumentation.[18] A laser 'maps' the sample surface by measuring spectra

at many spatial locations using a dispersive spectrometer or an interferometer. These instruments accomplish this either by moving the laser across the sample in point-by-point or line scanning mode. For point-by-point scanning, the sample is raster scanned through the focused laser beam, collecting the entire Raman spectrum at each point.[19] These spectra are then used to construct a three-dimensional hypercube or a Raman image.

The measurement time using point-by-point scanning has historically been long; dependent on the number of spatial points desired in the Raman image. In a Raman microprobe, the signal is frequently focused through a pinhole, known as a confocal arrangement, in order to restrict the collection volume. A disadvantage of this is that up to 98% of the generated Raman signal is not collected, so the exposure time at each point must be increased for confocal systems.[20] Additionally, longer measurement times may be necessary if photobleaching is required to quench sample fluorescence, but one must also be careful to avoid laser-induced sample damage. In the past, the time to measure a Raman image this way could be anywhere from hours to days, but due to advancements in commercially available scanning probe technology the acquisition time for a single Raman spectrum can be on the order of microseconds, acquiring hundreds of Raman spectra per second.[17] The spatial resolution is limited by the laser spot size as well as the mechanics of the rastering stage.

In line scanning, the laser is focused to a thin line using cylindrical optics. The illumination line on the sample is parallel to the entrance slit of a dispersive spectrometer so that a Raman spectrum is acquired on each row of a two-dimensional array detector.[21] Using this method, the sample needs to be raster scanned in only the dimension perpendicular to the illumination line. Line scanning allows measurement times to be

proportional to the square root of the number of rows of pixels in the Raman image; an improvement over point-by-point scanning methods. This improvement is only possible if there is adequate laser power to maintain a laser power density comparable to that of point-by-point methods. The spatial resolution of line scanning methods is different in the X and Y dimensions. Spatial resolution in the direction perpendicular to the laser line depends on the laser beam width and the mechanics of the rastering stage. In the direction parallel to the laser line the spatial resolution depends on the magnification of the collection optics and the pixel size of the detector. There are high performance line scanning Raman imagers available commercially.

1.6.2 WIDE FIELD METHODS

Further advancements in Raman imaging technologies have led to wide-field Raman imaging techniques; where all points on the sample are measured simultaneously using an expanded laser spot while a single Raman band is measured using a tunable filter to acquire a 2D Raman image. The hyperspectral image is built up by measuring Raman images as the filter is tuned to different Raman bands. The acquisition time is proportional to the number of spectral channels being analyzed instead of the number of pixels in the Raman image as with scanning methods. For many applications, only a small number of spectral bands are required for sufficient characterization, so real time Raman imaging is feasible.[22,23] High spatial resolution can be obtained with wide field Raman imaging as it is limited by the resolution of the CCD. The utility of these techniques has been demonstrated for applications including pharmaceuticals and homeland security.[23,24]

Tunable lasers, dielectric filters, acousto-optic tunable filters and liquid crystal tunable filters have all been demonstrated as useful for Raman imaging. Raman imaging with

dielectric interference filters was demonstrated in the early 1990's when Batchelder et al. used dielectric interference filters with ~20 cm^{-1} passbands on a mechanically rotating wheel.[25] Images were taken of the globally illuminated sample using each of the different filters. Some advantages of this technique are near diffraction limited spatial resolution and simplicity of instrumentation. However, image shift associated with filter movement is an issue. Another variation of this technique is to use a stationary dielectric filter with a tunable laser to excite Raman.[26] This overcomes the filter movement issue but has challenges related to rejection of Rayleigh scatter.

Acoustoopic tunable filters were first demonstrated in the early 1990's. These stationary, solid state filters diffract different narrow spectral bandpasses of light by applying an rf signal to the filter. In an anisotropic crystal medium, an acoustic soundwave interacts with the light traveling through it.[27] This technique allows for broad spectral coverage and fast tuning speeds, but low spectral resolutions, on the order of 50 cm^{-1}, is a limitation for Raman imaging. Even so, this type of instrumentation has been demonstrated for many applications, including remote Raman imaging.[28]

Liquid crystal imaging spectrometers can provide spectral resolution similar to that of a single dispersive monochromator with near diffraction-limited spatial resolution, but suffer from moderate light throughput.[29] There are many types of liquid crystal tunable filters (LCTF). The first LCTF was introduced by Lyot as fixed retardance birefringent materials bonded to a nematic liquid crystal wave plate and oriented between two parallel linear polarizers.[30] Layering Lyot filters creates a narrow passband due to combined constructive and destructive interference. A bandpass of 7.6 cm^{-1} can be achieved and is continuously tunable by applying voltage to the liquid crystal waveplate. A drawback of

these filters is low light throughput; as many polarizers must be layered with resultant high transmission losses.

The next development in LCTF happened with the invention of the Solc filter. Only two polarizers are used in this design, so there is an improvement in light throughput.[31] However, this filter is not recommended for Raman imaging because this design has poor out-of-band rejection efficiency.[32] To improve on this, Evans introduced a filter that balances throughput and rejection efficiency. The Evans split element filter maintains a narrow bandpass (9 cm^{-1}) while doubling the optical throughput as compared to the original Lyot filter.[33] This technology was considered the state-of-the-art for wide field Raman imaging throughout the 1990s and early 2000s, but the need for even higher light throughput arose for applications involving extremely low light imaging.[17]

Lastly, Fabry-Perot LCTF imaging spectrometers have been used for Raman imaging. These spectrometers provide moderate spectral resolution (20 cm^{-1}) and high image quality, but some limitations include small acceptance angle, limited spectral range, and low out-of-band rejection.[34]

Fiber array spectral translators (FAST) reduce two spatial dimensions of data to a single dimension, allowing rapid analysis in applications where a wide range of spectral information is needed over a small spatial area. A two-dimensional array of fibers collects signal from the globally illuminated sample and translates it into a linear array that is fed into the entrance slit of a dispersive spectrometer with an imaging format CCD.[35] Software is used to reconstruct the data to a hyperspectral cube. Some challenges of FAST include manufacturability of the fiber arrays as well as pixel-to-pixel crosstalk. This technique also provides a relatively small number of spatial points to be measured, on the order of a few

hundred.[35] FAST bundles have been demonstrated for many applications.

1.7 REFERENCES

1.National Academies of Sciences, Engineering, and Medicine. 2011. Visions and Voyages for Planetary Sciences in the Decade 2013-2022. Washington, DC: The National Academies Press.

2.D. A. Rusak, B. C. Castle, B. W. Smith, J. D. Winefordner. "Fundamentals and applications of laser-induced breakdown spectroscopy". Critical Reviews in Analytical Chemistry. 1997. 27(4): 257-290.

3.E. Tagnoni, V. Palleschi, M. Corsi and G. Christoforetti. "Quantitative micro-analysis by laser-induced breakdown spectroscopy: a review of the experimental approaches". Spectrochim. Act. B. 2002. 57: 1115-1130.

4.D. A. Cremers and L. J. Radziemski. Handbook of Laser-Induced Breakdown Spectroscopy. 2013. West Sussex, United Kingdom: Wiley & Sons, Ltd.

5.Y. Deguchi and Z. Wang. "Industrial Applications of Laser-Induced Breakdown Spectroscopy". Plasma Science and Technology. InTechOpen. 2015. DOI: 10.5772/60692.

6.W. Li, X. Li, X. Li, Z. Hao, Y. Lu and X. Zeng. "A review of remote laser-induced breakdown spectroscopy". Applied Spectroscopy Reviews. 2018. 1-25.

7.A. K. Knight, N. L. Scherbarth, D. A. Cremers and M. J. Ferris. "Characterization of Laser-Induced Breakdown Spectroscopy (LIBS) for Application to Space Exploration". Appl. Spectrosc. 2000. 53(3): 331-340.

8.R. C. Wiens, S. Maurice, et. al. "The ChemCam Instrument Suite on the Mars Science Laboratory (MSL) Rover: Body Unit and Combined System Tests". Space Sci. Rev. 2012. 170: 167-227.

9.S. Maurice, R. C. Wiens, et. al. “The ChemCam Instrument Suite on the Mars Science Laboratory (MSL) Rover: Science Objectives and Mast Unit Description”. Space Sci. Rev. 2012. 170: 95-166.

10. R. C. Wiens, S. Maurice and F. R. Perez. “The SuperCam Remote Sensing Instrument Suite for the Mars 2020 Rover: A Preview”. Spectroscopy. 32(5): 50-55.

11. S. M. Angel, S. K. Sharma, N. R. Gomer, and C. McKay. “Remote Raman Spectroscopy for Planetary Exploration: A Review”. Appl. Spectrosc. 2012. 66: 137-150.

12. C. V. Raman. “A Change of Wave-Length In Light Scattering”, Nature, 1928. 121: 619.

13. J. D. Ingle and S. R. Crouch. Spectrochemical Analysis. 1988. Englewood Cliffs, NJ: Prentice-Hall International Editions.

14. J. S. Greer, G. I. Petrov, V. V. Yakovlev. “Raman spectroscopy with LED excitation source”. J. Raman Spectroscopy. 2013. 44: 1058-1059.

15. P. Magnan. “Detection of visible photons in CCD and CMOS: A comparative view”. Nucl. Instrum. Meth. A. 2003. 504: 199-212.

16. A. H. Titus, M. Cheung, and V. P. Chodavarapu, V. Photodiodes-World Activities in 2011: Chapter 4 “CMOS Photodetectors”. InTech. 2011.

17. S. Stewart, R. J. Priore, M. P. Nelson and P. J. Treado. “Raman Imaging”. Annu. Rev. Anal. Chem. 2012. 5: 337-360.

18. M. Delhaye and P. Dhamelincourt. “Raman microprobe and microscope with laser excitation”. J. Raman Spectrosc. 1975. 3: 33-34.

19. L. Boogh, R. Meier, and H. Kausch. “A Raman microscopy study of stress transfer in high-performance epoxy composites reinforced with polyethylene fibers”. J. Polym. Sci.

B. 1992. 30: 325-333.

20. C. Brenen and I. Hunter. “Chemical imaging with a confocal scanning Fourier transform Raman microscope”. Appl. Opt. 1994. 33: 7520-7528.
21. M. Bowden, D. Gardiner, G. Rice, D. Gerrand. “Line-scanned micro Raman spectroscopy using a cooled CCD imaging detector”. J. Raman Spectrosc. 1990. 21: 37-41.
22. P. J. Treado, I. W. Levin, E. N. Lewis. “Near-infrared acousto-optic filtered spectroscopic microscopy: a solid state approach to chemical imaging”. Appl. Spec. 1992. 46(4): 553-559.
23. W. Doub, W. Adams, J. Spencer, L. Buhse, M. Nelson, and P. Treado. “Raman chemical imaging for ingredient specific particle size characterization of aqueous suspension nasal spray formulations: a progress report”. Pharm. Res. 2007. 24: 934-945.
24. G. Mogilevsky, L. Borland, M. Brickhouse, A. W. Fountain III. “Raman Spectroscopy for homeland security applications”. Int. J. Spectrosc. 2012. 2012: 1-12.
25. D. N. Batchelder, C. Cheng, W. G. D. Pitt. “Molecular imaging by Raman microscopy”. J. Adv. Mater. 1991. 3(11): 566-568.
26. G. Puppels, M. Grond, J. Greve. “Direct imaging Raman microscope based on tunable wavelength excitation and narrow-band emission detection”. Appl. Spectrosc. 1993. 47: 1256-1267.
27. P. Treado, I. Levin, E. Lewis. “High-fidelity Raman imaging spectrometry: a rapid method using an acousto-optic tunable filter”. Appl. Spectrosc. 1992. 46:1211-1216.
28. H. Skinner, T. Cooney, S. Sharma, and S. M. Angel. “Remote Raman microimaging using an AOTF and a spatially coherent microfiber optical probe”. Appl. Spectrosc.

1996. 50: 1007-1014.

29. H. Morris, C. Hoyt, P. Miller, P. Treado. “Liquid crystal tunable filter Raman chemical imaging”. Appl. Spectrosc. 1996. 50: 805-811.

30. B. Lyot. “The birefringent filter and its application in solar physics”. Ann. Astrophys. 1944. 7: 3136.

31. I. Solc. “Birefringent chain filters”. J. Opt. Soc. Am. 1965. 55: 621-625.

32. S. Saeed and P. Bos. “Multispectrum, spatially addressable polarization interference filter”. J. Opt. Soc. Am. A. 2002. 19: 2301-2312.

33. J. Evans. “The birefringent filter”. J. Opt. Soc. Am. 1949. 39: 229-237.

34. K. Christensen, N. Bradley, M. Morris, R. Morrison. “Raman imaging using a tunable dual-stage liquid crystal Fabry-Perot interferometer”. Appl. Spectrosc. 49: 1120-1125.

35. J. Ma and D. Ben-Amotz. “Rapid micro-Raman imaging using fiber-bundle image compression”. Appl Spectrosc. 1997. 51: 1845-1848.

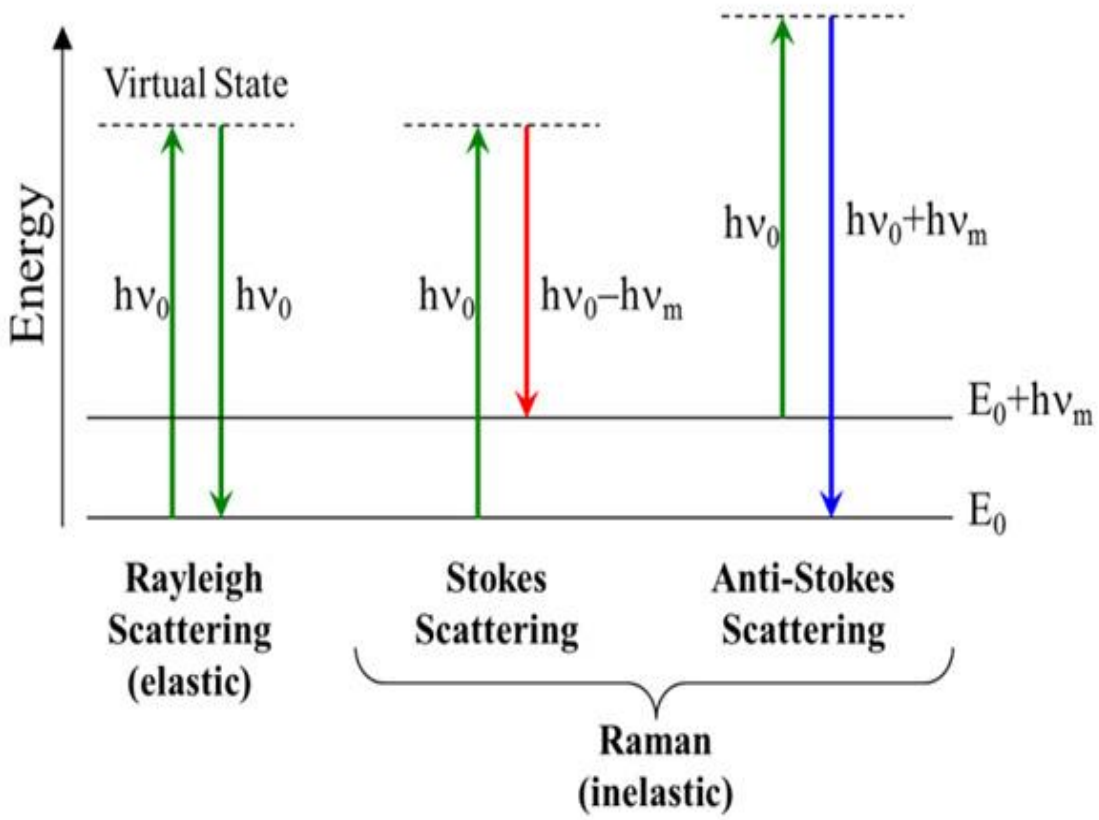

Figure 1.1 Energy level diagram showing quantum energy transitions for Rayleigh and Raman scattering. The energy changes that produce stokes and anti-Stokes scattering are depicted on the right. The two differ from the Rayleigh scatter by frequencies corresponding to ν_m, the energy of the first vibrational level of the ground state.

CHAPTER 2

SPATIAL HETERODYNE SPECTROSCOPY

2.1 GENERAL OVERVIEW

The spatial heterodyne spectrometer (SHS), developed by Harlander in 1990, was first used for the collection of Raman spectra in 2011 by Gomer et. al.[1-4] Since its development it has been demonstrated for use in standoff Raman and LIBS, deep-ultraviolet Raman, and with the use of a miniature cell-phone complementary metal-oxide semiconductor (CMOS) detector.[4-11] In this text, the SHS is used for analyzing Raman and LIBS signals, and these are further referred to as spatial heterodyne Raman spectrometer (SHRS) and spatial heterodyne LIBS spectrometer (SHLS).

The SHS, shown schematically in figure 2.1, is a wide-field, high resolution Fourier transform (FT) interferometer with no moving parts and no entrance slit. It provides 100-200 times higher light throughput than a dispersive spectrometer of comparable resolution, and spectral resolution is not strongly dependent upon entrance aperture size.[1,2] The SHS can be tuned to any wavelength and can be built monolithically with potential for miniaturization. These qualities make it an interesting device with significant potential for space applications.

2.2 SHS WORKING PRINCIPLE

The signal of interest is collected, collimated, and sent through the input aperture where it is split into two beams by a 50/50 transmission beam splitter. When these two beams strike the stationary, tilted diffraction gratings, a wavelength dependent tilt is introduced to the wavefronts as they are diffracted back down the same path. They reenter the beam splitter and recombine producing an interference pattern that is imaged onto an imaging detector. The intensity of the fringe pattern is a function of position, *x*, on the detector given by Eq. 2.1:

$$I(x) = \int B(\sigma)\{1+\cos[8\pi\,(\sigma-\sigma_L)x\,\tan\theta_L]\}d\sigma \qquad \text{Eq. 2.1}$$

Where $B(\sigma)$ is the input spectral intensity at wavenumber σ, and the Fourier transform of $I(x)$ recovers the Raman spectrum. The grating tilt, or Littrow angle, Θ_L, sets the heterodyned, or Littrow wavenumber, σ_L, that corresponds to zero spatial frequency according to Eq. 2.2:

$$\theta_L = \mathrm{Sin}^{-1}(m/2d\sigma_L) \qquad \text{Eq. 2.2}$$

where d is diffraction grating groove spacing and m is the diffraction order (generally one). The interference pattern produces an image of vertical, wavelength dependent fringes of spacing f_x, defined by Eq. 2.3:

$$f_x = 4(\sigma - \sigma_L)\tan\theta_L \qquad \text{Eq. 2.3}$$

where σ is the wavenumber of the Raman band. For the SHS equipped with gratings of width, W, and D grooves per millimeter, the maximum theoretical resolving power, R, is determined by the number of grating grooves illuminated as given by Eq. 2.4:

$$R = 2\,W\,D = (\lambda/\Delta\lambda) \qquad \text{Eq. 2.4}$$

where λ is the center wavelength and $\Delta\lambda$ is the smallest resolvable wavelength difference that can be measured by the spectrometer. For the SHS, the number of spectral elements recovered, $N/2$, is determined by the number of detector elements in the x-direction, N, according to the Nyquist criterion. This allows for high spectral resolution to be achieved with a relatively small number of samples over a maximum theoretical spectral range given by Eq. 2.5:

$$\text{Maximum Theoretical Bandpass} = (N\,\lambda) / (2\,R) \qquad \text{Eq. 2.5}$$

The actual spectral range is generally slightly less than theoretical because the SHS response function drops off quickly for signals further from Littrow. Imperfect focusing,

optical abberations and detector characteristics can also contribute to decreased spectral range. Light throughput or entendue, *E*, is given by Eq. 2.6:

$$E = A\,\Omega \qquad \text{Eq. 2.6}$$

Where *A* is the area viewed given by the entrance aperature and Ω is the collection solid angle of the SHS given by Eq. 2.7:

$$\Omega = (2\,\pi) / R \qquad \text{Eq. 2.7}$$

The full-angle field of view is equal to the square root of Ω; usually around 1° for the SHS. This field of view can be increased by incorporating field-widening prisms in each arm of the SHS.[2] The large entrance aperture simplifies the alignment required for standoff Raman/LIBS and provides high light throughput allowing large spot sizes and extended illumination sources to be used on the sample without a loss of signal or resolution.[5-7]

The SHS is subject to the shortcomings of all interferometers. It gains a partial multiplex advantage by measuring all wavelengths simultaneously, but a disadvantage to this is the equal distribution of noise throughout the entire spectrum. Additionally, because the SHS distributes the interferogram over many detector elements, distortions can arise if the detector channels are not carefully cross-calibrated. Interferometers are extremely sensitive to vibrations of the optics with respect to one another. However, operation with no moving parts allows the SHS to be built monolithically, and the only critical alignment is that the optical path length between the two gratings must be within the coherence length of the collected light given by Eq. 2.8:

$$l = \lambda^2 / (n\,\Delta\lambda) \qquad \text{Eq. 2.8}$$

where *l* is the coherence length, λ is the center wavelength, $\Delta\lambda$ is the spectral bandwidth in terms of wavelength and *n* is the refractive index of the propagating material. The natural

linewidth of a Raman band is generally between 1-10 cm^{-1}, (with exceptions) depending on the sample. The coherence lengths in fused silica (n =1.46 @ 532 nm) for Raman bands with 10 cm^{-1}, 5 cm^{-1}, and 1 cm^{-1} linewidths are ~0.7 mm, ~1.4 mm and ~7 mm respectively. This is large enough that precision machining of mounts or a monolithic device is adequate for alignment of most components and makes the system sturdy and tolerant to disturbances it would feel during space travel.

2.3 SHS DATA PROCESSING

The SHS interferogram is imaged onto a detector and digitally converted to the image file. To retrieve the spectrum, the columns of the fringe image are summed in the vertical direction to provide a interferogram superimposed on a background signal. The magnitude of the background signal varies from sample to sample and is made up of a combination of out of band Raman, emission, luminescence and ambient background light. There is also a dc background component inherent to the interferometer. The background subtracted interferogram is obtained by subtracting the background, usually obtained by fitting a high order polynomial to the interferogram to obtain the dc component. The spectrum is obtained by performing the 1D fast Fourier transform on the background subtracted interferogram.

In some cases, an alternate form of background subtraction is performed. Instead of fitting a polynomial, a series of measurements are made with the SHS to obtain the dc component specific to that measurement. To do this, the raw image file, I_{raw}, and three background images are taken under the same acquisition settings. Using pieces of opaque material, each grating is blocked individually to measure I_{g1b} and I_{g2b}, respectively; then both gratings are blocked to obtain the third background image, I_{bgb}. The background

corrected interferogram, I_{bksb}, is then given by Eq. 2.9:

$$I_{bksb} = I_{raw} - (I_{g1b} + I_{g2b}) + I_{bgb} \quad \text{Eq. 2.9}$$

Interferogram apodization is used as needed to smooth ringing artefacts observed in the spectral domain. These artefacts appear in cases where the fringe image overfills the detector, causing the interferogram to be terminated in a square fashion. When the fringe image does not overfill the detector, the interferograms are self-apodizing; i.e. smoothly truncated. The ringing is caused by interferogram truncation effects and many different apodization functions exist. After investigating the available functions, the Hamming apodization function showed best performance. The Hamming function is multiplied by the interferogram prior to fast Fourier transform (FFT). In cases where fringe tilt degrades the contrast of the interferogram cross section, the spectrum can be obtained via a row-wise discrete fast Fourier transform (FFT) according to that documented by Barnett.[10]

2.4 SHS FIGURES OF MERIT

The signal-to-noise ratio (SNR) of the Raman peaks in a spectrum characterizes the quality of the Raman spectrum. SNR is equal to the baseline corrected signal divided by the noise. Baseline corrected signal is obtained by taking the average of the two lowest intensity points on either side of the peak of interest and subtracting this average from the raw intensity of the peak. Noise is calculated as the standard deviation over a pixel region containing only baseline. For a detector limited by shot noise, the noise can be estimated as the square root of the signal. The quality of the interferogram is characterized by its contrast, or fringe visibility, *FV*, given by Eq. 2.10:

$$FV = (I_{max} - I_{min}) / (I_{max} + I_{min}) \quad \text{Eq. 2.10}$$

where I_{max} and I_{min} are the maximum and minimum signal intensities of the interferogram

modulation. Maximum theoretical FV is 1, and the SHS has achieved FV as high as 0.8 in our lab. Vibrational interferences, stray light, imaging issues, dust and misalignment are factors that decrease FV. Viable spectra have been obtained with FV as low as 0.007.

2.5 SHRS SIGNIFICANCE FOR PLANETARY EXPLORATION

Spatial heterodyne Raman spectrometers have useful characteristics for planetary exploration. No moving parts means it can be built monolithically, making it rugged for field applications. The SHRS is compatible with pulsed excitation and gated detection, a necessity for LIBS and an advantage for Raman. The wide entrance aperture allows for a wide field of view and high optical throughput. The SHRS is capable of high resolving power, proportional to grating line density, over spectral range proportional to the number of detector elements. The SHS can be tuned to any wavelength and is compatible with the deep UV. Because the resolving power is independent of focal length, the SHS can be miniaturized without sacrificing spectral resolution. Taken all together, these qualities give some interesting possibilities.

The field of view of the SHRS is much larger than that of traditional spectrometers. The large field of view of the SHRS is important for remote measurements because it eases alignment restrictions and makes it more tolerant of laser shot to shot pointing jitter. This opens the door to applications like drone-mounted optics. The large field of view allows for an expanded beam to illuminate the sample. Not only helpful for avoiding photodegradation, the large entrance aperture makes the SHRS compatible with large format microlens arrays for hyperspectral imaging. It is also useful for diffuse sources like those encountered in transmission and spatially offset Raman.

2.6 REFERENCES

1. J. M. Harlander, F. L. Roesler and S. Chakrabarti. “Spatial Heterodyne Spectroscopy: A Novel Interferometric Technique for the FUV”. EUV, X-Ray and Gamma-Ray Instrumentation for Astronomy, O. H. W. Siegmund; H. S. Hudson, Eds.; Proceedings of the SPIE. 1990. 1344: 120-131.
2. J. M. Harlander, Spatial Heterodyne Spectroscopy: Interferometric Performance at Any Wavelength without Scanning. Ph.D. Thesis, University of Wisconsin-Madison. 1991.
3. J. M. Harlander, F. L. Roesler, R. J. Reynolds, K. Jaehnig and W. A. Sanders. “Differential, Field-Widened Spatial Heterodyne Spectrometer for Investigations at High Spectral Resolution of the Diffuse Far Ultraviolet 1548 Å Emission Line from the Interstellar Medium”. In Proceedings of the SPIE. 1993. 2006: 139-148.
4. N. R. Gomer, C. M. Gordon. P. Lucey, S. K. Sharma, J. C. Carter and S. M. Angel. “Raman Spectroscopy Using a Spatial Heterodyne Spectrometer: Proof of Concept”. Appl. Spectrosc. 2011. 65(8): 849-857.
5. N. Lamsal and S. M. Angel. “Deep-Ultraviolet Raman Measurements Using a Spatial Heterodyne Raman Spectrometer (SHRS)”. Appl. Spectrosc. 2015. 69(5): 525–534.
6. N. Lamsal, S. M. Angel, S. K. Sharma and T. E. Acosta. “Visible and UV Standoff Raman Measurements in Ambient Light Conditions Using a Gated Spatial Heterodyne Raman Spectrometer”. 46th Lunar and Planetary Science Conference. 2015. Woodland TX. March 16-20, 2015.
7. N. Lamsal, S. K. Sharma, T. E. Acosta and S. M. Angel. “Ultraviolet Stand-off Raman Measurements Using a Gated Spatial Heterodyne Raman Spectrometer”. Appl. Spectrosc. 2016. 70(4): 666–675.

8. I. B. Gornushkin, B. W. Smith, U. Panne and N. Omenetto. “Laser-Induced Breakdown Spectroscopy Combined with Spatial Heterodyne Spectroscopy”. Appl. Spectrosc. 2014. 68(9): 1076-1084.
9. P. D. Barnett and S. M. Angel. “Miniature Spatial Heterodyne Raman Spectrometer with a Cell Phone Camera Detector”. Appl Spectrosc. 2017. 71(5): 988-995.
10. P. D. Barnett. The Development of a Miniature Spatial Heterodyne Raman Spectrometer for Applications in Planetary Exploration and Other Extreme Environments. Ph.D. Thesis, The University of South Carolina- Columbia, 2016.
11. M. J. Egan, S. M. Angel and S. K. Sharma. “Standoff spatial heterodyne Raman spectrometer for mineralogical analysis”. J. Raman Spectrosc. 2017. 48: 1613–1617.

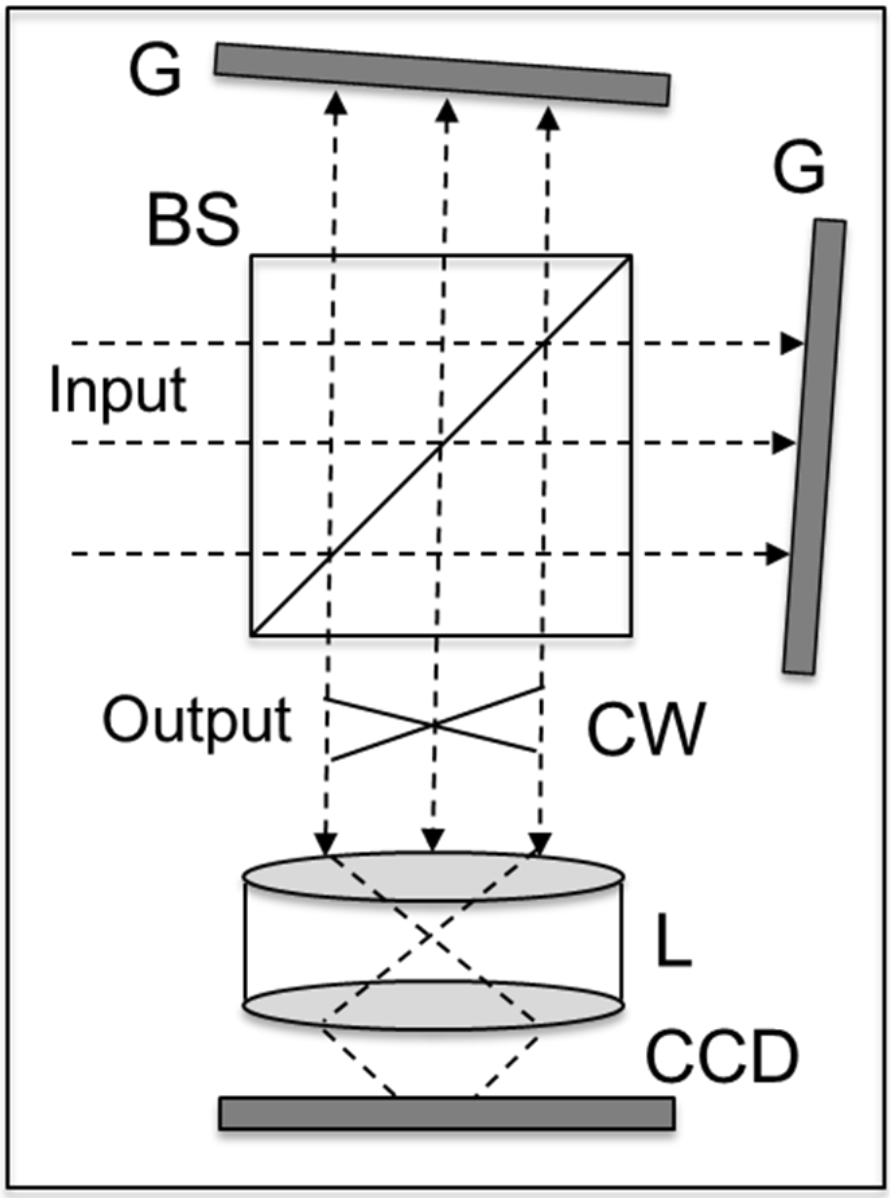

Figure 2.1 (A) Spatial heterodyne spectrometer. BS=beam splitter, G=diffraction grating, CW=crossing wavefronts, L=lens, CCD= charge coupled device detector.

CHAPTER 3

MINIATURE SPATIAL HETERODYNE SPECTROMETER FOR REMOTE LASER-INDUCED BREAKDOWN AND RAMAN SPECTROSCOPY USING FRESNEL COLLECTION OPTICS[A]

[A]Allen, A. and Angel, S. M. 2018. *Spectrochimica Acta Part B: Atomic Spectroscopy.* 149: 91-98. Reprinted here with permission of publisher.

3.1 ABSTRACT

A combined laser-induced breakdown (LIBS) and Raman, spatial heterodyne spectrometer (SHLS/SHRS) is described for remote measurements using Fresnel collection optics. The spatial heterodyne LIBS and Raman spectrometer (SHLS and SHRS) is based on a fixed diffraction grating interferometer with no moving parts that offers a very large field of view, high light throughput, and high spectral resolution in a small package. The field of view of the SHS spectrometer is ~1° making it very forgiving of collection optics alignment and image quality for remote LIBS and Raman measurements. In the SHLS/SHRS system described here, a ~100-mm diameter, f/1.25 Fresnel lens used for light collection is compared to a high quality ~100-mm aperture Questar long distance microscope. LIBS and Raman measurements were made at 10 m for a variety of organic and mineral samples including materials from deep ocean hydrothermal vents.

3.2 INTRODUCTION

The spatial heterodyne spectrometer (SHS) is an interferometer that has characteristics that are well suited for remote LIBS and Raman. Like other interferometers, the SHS has a very high light throughput and a wide field of view but also has very high spectral resolution. In addition, the SHS design has no moving parts making it compatible with a gated detector necessary for remote LIBS. The SHS, first described by Harlander,[1,2] is similar to a Michelson interferometer but the interference pattern is formed on an imaging detector using stationary, rotated diffraction gratings, thus there are no moving parts. The grating rotation angle determines the Littrow wavelength, which is the wavelength about which all others are heterodyned. Heterodyning allows high spectral

resolution to be achieved with a relatively small number of samples, fixed by the number of horizontal pixels on the imaging detector. The large entrance aperture and wide acceptance angle of the SHS provides high light throughput for extended sources, at least two orders of magnitude higher than a conventional dispersive spectrometer.[1]

The first description of a laser based, gated SHS spectrometer was for visible Raman spectroscopy[3], and later for UV Raman[4,5] and remote Raman,[5,6] and most recently for LIBS.[7] In the case of standoff LIBS and Raman, the wide acceptance angle and large aperture makes the SHS relatively easy to couple with telescopic optics and minimizes laser pointing stability issues, because small movements of the laser spot on the target do not reduce the amount of light collected by the spectrometer aperture, unlike the case of a dispersive spectrometer where the output of the telescope has to be held in focus on a narrow input slit.[6] In addition, all wavelengths are measured simultaneously in the SHS, making it compatible with pulsed lasers and gated detection, necessary in remote LIBS and Raman to reduce background.

The 2013 Planetary Decadal Survey recommends a high priority be placed on remote sensing technology with a focus on developing and maturing novel, crosscutting, low-mass/power sensors integrated into robust, low-cost system architectures.[8] Growing interest in the development of autonomous chemical measurement systems looks toward the CubeSat design. The CubeSat has a standard size and form factor; the smallest unit, 1U, measures 10x10x10 cm^3 and weighs less than ten kilograms, and these units can be combined up to a 12U size.[9] We are exploring remote Raman and LIBS instrumentation that might fit the CubeSat architecture. The SHS spectrometer and collection optics should ideally fit in a 1U unit, however multiple units might be used for different components such

as the laser, detector, and power supplies. In the case of Raman, a small diode laser light source along with a small CMOS detector, similar to one we demonstrated recently in a cell-phone based SHRS spectrometer,[10,11] might allow the entire spectrometer to fit a 1U unit. Even in the case of LIBS, there are small pulsed lasers that are ideally suited to a 1U architecture.[12]

The SHS spectrometer design is ideal for small CubeSats because of the small size of the spectrometer. However, for remote spectroscopy large collection optics are required with short focal lengths to fit the 10 cm CubeSat dimensions (~f/1). Conventional f/1 lenses and mirrors are very thick and heavy and are not amendable. Large ~f/1 Fresnel optics on the other hand are very thin (e.g., 1-2 mm) and light weight. A Fresnel lens is a thin, flat piece of optical material having a series of grooves that approximate the spherical surface of a conventional lens. They are lightweight, cheap, and widely used for magnification and light collection, but image quality suffers due to increased scattering at the grooves.[13] Fresnel optics would seem to be ideal candidates as large aperture collectors in CubeSat remote spectrometers. Fresnel lenses have not been documented for the collection of Raman or LIBS spectra. In the following we describe a combined remote LIBS and Raman spatial heterodyne spectrometer, using Fresnel collection optics.

3.3 EXPERIMENTAL

For the continuous wave (CW) excitation Raman experiments, a frequency doubled 532 nm Nd:YAG laser (SpectraPhysics, Inc., Millenia Pro) was used to illuminate the sample. The beam diameter at the sample at 10 meters is about 6-7 mm. Laser power was 0.22 W for sulfur and 0.75 W for potassium perchlorate. Acquisition times of 7 seconds for sulfur and 60 seconds for potassium perchlorate were used. For pulsed excitation, a Q-

switched, frequency doubled Nd:YAG laser (Continuum Surelite III) was used to generate 532 nm laser pulses with a pulse width of 7 ns. The sample was illuminated from an angle of about 15^{o} relative to the optical axis of the collection optics and spectrometer. The laser was operated at 1 Hz using 124 mJ/pulse for LIBS studies, and at 5 Hz using 24.9 mJ/pulse for Raman measurements. A beam expander was used to defocus the beam to ~10 mm on the sample for Raman measurements. For LIBS measurements the laser was focused to a small spot in order to form the LIBS plasma.

The SHS interferometer consists of a 25 mm N-BK7 non polarizing 50:50 cube beamsplitter (Thorlabs BS013) and a pair of 150 grooves/mm, 25 mm square diffraction gratings blazed at 500 nm (Edmund optics #64-402). For Raman measurements, a 532 nm longpass filter (Semrock RazorEdge, LP03-532RE-25) and 600 nm shortpass filter (Thorlabs FES600) were used to remove strong Rayleigh scatter from the laser and to keep incoming signal within the SHS spectral range. An iris at the input aperture limited the size of the illuminated area on the gratings to 20 mm. For LIBS measurements, a 532 nm holographic notch filter (Kaiser Optical Systems, HSPF-532.0-2.0) was used instead of the 532 nm longpass filter. The interferogram was imaged onto the detector using a Nikon AF-S Nikkor 80-200 mm f/4.6G ED VRII lens (Nikon, Tokoyo, Japan) placed about 160 mm from the grating face on focal setting 105 mm. A spatial filter placed one focal length from the imaging lens was used to block higher grating orders. The detector was a thermoelectrically cooled 1024x253 gated ICCD array detector having 26 micron pixels (Princeton Instruments, Model PIMAX4). The ICCD gate width and delay time were optimized for each LIBS sample to give best interferogram quality as measured by the signal to background. Fourier transform of interferogram images was carried out in

MATLAB to recover the spectrum. No apodization, flat field or instrument response corrections, or any other post processing were performed. Comparison LIBS spectra were measured using an Ocean Optics, LIBS-2000+ spectrometer with a 1064 nm laser. The sample chamber used 7, ~333 micron optical fibers for collection, placed approximately 25 mm from the surface of the sample (~f/75). Samples were excited with 200 mJ laser pulses at 1 Hz repetition rate, and 7.83 ns pulse width. The Q-switch delay was set to -20 us, where the negative sign means the Q-Switch is being fired before the aperture has opened. 100 shots with 2.1 ms integration time were averaged to produce the spectra.

Signal collection for standoff experiments used a two lens scheme, a 'collector' that collects light from the sample and a 'collimator' that collimates the collected light and sends it into the SHS spectrometer. The collimator lens also matches the beam size to the SHS spectrometer input aperture.

For these experiments, the collection efficiency of a 102 mm diameter, 1 mm thick acrylic Fresnel lens with focal length 127 mm (Knight Optical, LFG127102) was compared to that of a ~100-mm diameter Questar long distance microscope with 1300 mm effective focal length (Company Seven, Questar FR-1 MKIII model no. 33003/33024). A 25 mm diameter f/1 anti-reflection (AR) coated aspheric lens was used to collimate the collected signal into the SHS.

Sulfur (J.T. Baker) and Potassium perchlorate (Fisher Science) pellets were prepared using a die press. Calcite, quartz, gypsum, olivine, pyrite, barite, and malachite samples were obtained from an Introductory Earth Science Collection (American Educational, #1201-000). Mineral samples were washed in acetone prior to measurement. The hydrothermal vent samples and their elemental analysis were provided by Dr. Susan

E. Humphris, Senior Scientist in the Geology and Geophysics Department at Woods Hole Oceanographic Institution.

3.4 RESULTS AND DISCUSSION

The SHS, depicted in Figure 3.1A, is similar in construction to a Michelson interferometer with the mirrors replaced by stationary reflective diffraction gratings**.** The diffraction gratings are tilted such that one particular wavelength, the Littrow wavelength, is retro-reflected along the incident light path and recombines at the beamsplitter**.** The grating tilt, known as the Littrow angle, θ_L, sets the heterodyned Littrow wavenumber, σ_L, that corresponds to zero spatial frequency according to Eq. 3.1, where d is the diffraction grating groove spacing and m is the grating order.

$$\theta_L = \sin^{-1}(m/2d\sigma_L) \qquad \text{Eq. 3.1}$$

For any wavelength other than Littrow, the diffracted light leaves the gratings at an angle to the optical axis, resulting in crossed wavefronts, inducing a spatial phase shift, and generating an interference pattern, which produces a series of wavelength dependent fringes on the array detector. The fringe frequency on the detector is given by Equation 3, where f is in fringes/cm and σ is the wavelength expressed in wavenumbers.[14] A Fourier transform of the interferogram recovers the spectrum. According to Equation 3.2, emission lines above or below the Littrow wavelength show identical fringe patterns and can lead to degenerate lines (i.e., line overlap). This degeneracy can be removed by tilting one of the gratings vertically, which induces a rotation to the fringes, in opposite directions above and below Littrow.[4] In this case, a 2 dimensional (2D) Fourier transform can be used to recover spectra above and below the Littrow wavelength unambiguously. This is very useful to double the spectral range of the SHS.

$$f = 4(\sigma - \sigma_L)\tan\theta_L \qquad \text{Eq. 3.2}$$

The SHS, like other Fourier transform interferometers, does not require a narrow slit to achieve high resolution as is common with dispersive spectrometers because there is only a weak dependence of resolution on entrance aperture width. This allows the SHS to employ very large entrance apertures, greatly increasing the throughput of the system, which is advantageous when signal strength is low such as when the source is very far from the detector in a remote configuration.

In the SHLS/SHRS instrument described here, the resolving power is equal to the number of grooves illuminated, so in this case R = 6,000, giving a theoretical resolution of ~ 0.09 nm (3.1 cm^{-1}) at 532 nm. The active area of the ICCD is 18 mm or about 692 pixels so the theoretical spectral range of the SHLS/SHRS, based on the Nyguist criteria of 2 pixels per wavelength, is ~30 nm (~1073 cm^{-1}). The useful spectral range is only about 2/3 this value because the instrument response drops quickly at wavelengths far from the Littrow setting.[4] This spectral range can be doubled (~60 nm or 2145 cm^{-1}) by tilting one of the gratings slightly and using a 2D Fourier transform to recover wavelengths both above and below the Littrow wavelength, unambiguously. The maximum, resolution-limited solid angle field of view (FOV) of the SHS is related to the resolving power by Eq. 3.3.[1] Thus the solid angle FOV for this spectrometer is 8.4 x 10^{-4} sr, and the full acceptance angle is ~ 1.7°.

$$\Omega_{max} = 2\pi/R \qquad \text{Eq. 3.3}$$

Figure 3.1B shows examples of using the SHS for very high spectral resolution emission measurements using 25-mm, 600 gr/mm diffraction gratings, for Hg lamp emission and LIBS measurements of iron and copper (e.g., 112 pm, 80 pm, and 60 pm for

Hg, Fe and Cu, respectively). Note: 150 gr/mm gratings were used in the SHLS/SHRS system described below to acquire the data shown. Figure 3.2 shows how spectra are recovered from the SHLS/SHRS interference fringe images. A reference sample, sulfur, is used in this illustration. To retrieve the Raman spectrum, the columns of the fringe image are summed in the vertical direction to provide a raw interferogram superimposed on a background signal. The magnitude of the background signal varies from sample to sample, and is made up of a combination of out of band Raman, emission, luminescence and ambient background light. There is also a dc background component inherent to the interferometer. The background subtracted interferogram is obtained by subtracting the background, usually obtained by fitting a high order polynomial to the interferogram to obtain the dc component. The spectrum is obtained by taking the 1D Fourier transform of the background subtracted interferogram.

Figure 3.3A is a picture of a CubeSat and Fig. 3.3B shows how a fast collection lens as large as ~10 cm and a small SHS spectrometer can both be included in a 1U CubeSat architecture. In this scenario the laser can either be included in the 1U architecture, if small like a diode laser, or can be external in another part of the spacecraft. This also applies to the ICCD detector. For example, the SHS output might be coupled using a coherent fiber bundle to an ICCD that is located in a shielded part of the spacecraft. To fit the 1U architecture, a 10 cm collection optic must be ~f/1. Although large f/1 glass and quartz lenses, or mirrors, are available, they are typically very thick and heavy as shown by the f/1.5 lens in Fig. 3.3C. A comparable Fresnel lens is much thinner and lighter as shown in Fig. 3D. The Fresnel lens weighs less than 1% of the comparable glass lens. Obviously, the laboratory lasers and ICCD used in the studies described here are too large for a 1U

unit, but small pulsed lasers suitable for LIBS are available,[12] and small CMOS detectors have already been demonstrated using the SHRS.[10,11]

Figure 3.4 shows remote Raman spectra, using the CW 532 nm laser, of sulfur at 10 m using two different collection optics, a simple 102-mm diameter f/1.25 Fresnel lens (top) and a ~100-mm aperture Questar long distance microscope (lower). Both spectra are measured under otherwise identical conditions. The quality of the spectrum is determined by the interferometer characteristics and any background signal that is outside the bandpass of the interferometer (e.g., Rayleigh scatter, luminescence, ambient light, etc.). The intensity for the lower spectrum using the Questar is about 4 times higher than the intensity of the spectrum using the Fresnel lens, but both spectra have about the same fringe visibility (Eq. 3.4).

$$FV = (I_{max}-I_{min})/(I_{max}+I_{min}) \qquad \text{Eq. 3.4}$$

The insets show the interferograms for each collector type without background subtraction (raw interferogram, lower insets) and after background subtraction (upper insets). The FV for both spectra is about 0.3, calculated from the raw interferogram, and this value indicates that about 2/3 of the signal for both collection optics is from background, outside the interferometer bandpass and is not affected by the type of light collector. The unmodulated background signal is most likely Rayleigh scatter that is not completely blocked by the laser blocking filter, as well as any other background light that is outside the bandpass of the interferometer. The shape of the Fresnel interferogram also suggests nonuniform illumination on the interferometer gratings from Fresnel lens aberrations or misalignment. The measured spectral resolution is 10-11 cm^{-1} using either collection optic, higher than the 3.1 cm^{-1} theoretical, but this is not a result of the lower quality Fresnel lens.

The high NA of the Fresnel lens, f/1.25, makes it much more susceptible to misalignment compared to the Questar telescope. The throughput of Fresnel optics is reduced compared to conventional optics from high Fresnel reflection and scattering losses at the facets and severe chromatic aberrations. A factor of 4 loss by the Fresnel lens is not unexpected, however it might be acceptable in applications where weight and form factor are at a premium. The Fresnel is 0.15 cm thick and weighs ~220 g including the holder, the Questar is ~31 cm long and weighs ~5.4 kg.

The Fresnel lens is a thin optical material with series of grooves that approximate the spherical surface of a conventional lens. Conventional lenses with low f-numbers require high curvature making them thick, heavy and expensive to fabricate. Fresnel lenses are useful in applications where high light collection is desired in a low cost and low mass device. However, Fresnel lenses are subject to large optical aberrations, which include total internal reflection losses, facet scattering and facet blocking. For the lens used in this study, scattering losses were estimated to be ~15%. Design wavelength is also important to obtaining maximum concentration efficiency from a Fresnel lens. Wavelengths shorter than the design range are more inclined to be totally internally reflected and longer wavelengths are more apt to blocking losses. The Fresnel lens used in this study has a design wavelength of 670 nm, far from the wavelength range of use. This results in an estimated 2-fold increase in the size of the Airy disc for the lens used in this study (based on Zemax calculations) and thus lower throughput. Transmission losses occur at both the entrance and exit faces, and they increase with decreasing focal length.[13] An f/1.2 lens has combined (entry and exit) transmittance losses of 17%.[13] To account for additional combined loss due to facet blocking, groove defects and distorted lens material, 2% loss

for a 3.2 mm thick acrylic lens is reasonable.[13]

Figure 3.5 shows remote Raman spectra using the CW 532 nm laser of a $KClO_4$ pellet at 10 m using the Fresnel lens (top) and the Questar long distance microscope (lower) for collection. Both spectra are measured under otherwise identical conditions. Similar to the sulfur spectra in Fig. 3.4, the intensity measured using the Questar is about 4 times higher than the intensity of the spectrum measured using the Fresnel lens, and both spectra have about the same fringe visibility (see insets). The FV of ~0.09 indicates that about 90% of the signal for both collection optics is from background outside the interferometer bandpass or ambient light. The amount of background light seen here is almost identical to that seen for the sulfur sample, thus most of the background light does not seem to be from the sample and is likely from Rayleigh scattering. As in Fig. 3.4, the shape of the Fresnel interferogram also shows nonuniform illumination on the interferometer gratings. The measured spectral resolution is 9-10 cm^{-1} using either collection optic.

Figure 3.6 shows remote SHLS LIBS spectra for samples at 10 m, using a 100-mm, f/1.25 Fresnel collection lens, for two mineral samples, olivine (top spectrum, upper wavelength scale) and barite (middle spectrum, lower wavelength scale). Note: olivine lines appear below the SHS Littrow wavelength while barite lines appear above Littrow. The bottom barite LIBS spectrum was measured using the conventional Ocean Optics LIBS spectrometer. The inset shows the SHS interferograms for barite (lower) and olivine (upper). The FV of these spectra is low, about 0.007 for barite and 0.01 for the olivine sample (see inset), because the background signals were very high, most likely because bandpass limiting filters were not used in the interferometer to block Bremsstrahlung radiation, most of which occurs at wavelengths outside the bandpass of the interferometer.

However, the signal to noise ratio (SNR) of the LIBS spectrum is high for the olivine sample, about 365 for the ~517 nm line in the SHLS spectrum, estimating the noise as the baseline noise near the position of the line. This is a good way to estimate the noise in the SHLS spectrum since noise is equally distributed in the interferometer but is not a good way to estimate SNR for a dispersive spectrometer.

The SNR is ~204 for the same olivine sample measured using the Ocean Optics LIBS spectrometer with the sample ~0.1 m from the collection optic and all settings as close as possible to those used with the SHLS instrument. In this case noise cannot be approximated at the baseline because it is not equally distributed. An estimate of the noise was obtained by measuring back to back spectra, subtracting them and calculating the rms noise at the peak position, and dividing by sqrt(2) to take into account the increased noise resulting from the two spectral measurements that were made. The Ocean Optics spectrometer is not responsive in the spectral range shown so a line outside this range had to be used. This is a crude comparison because there are large differences in the instruments and the measurement conditions. When the sample distance (10 m versus 25 mm), size of the collection aperture (100 mm versus ~333 microns—f/100 versus f/75) and laser power (125 mJ versus 200 mJ, both ~7 ns pulse width) are taken into account, you would expect the intensity of the SHLS measured spectrum to be about 1/3rd $[(75^2/100^2)*(125/200)]$ that of the Ocean Optics system. Our measured sensitivity is in fact much higher for this sample, as indicated by a larger SNR for the SHLS spectrometer. Of course this assumes all else is equal which they clearly are not since there are large differences in the laser wavelength and spot size at the sample, the efficiency of the collection optics, the detector responses, the overall spectrometer throughput, background

contributions, sample plasma size and temperature, between the spectrometers, among other things.

Figure 3.7 shows remote SHS LIBS spectra using the pulsed 532 nm laser with a gated detector for the minerals malachite, gypsum and pyrite at 10 m using a 100-mm, f/1.25 Fresnel collection lens, compared to the same samples measured using the Ocean Optics LIBS spectrometer. SHS spectra are recorded using 100 laser shots, 2.3 us gate delay, 2 us gate width, and 124.5 mJ, 532 nm excitation. Below each SHS spectrum is the corresponding spectrum that was measured using the Ocean Optics spectrometer (marked Conv). Most lines shown appear below the Littrow wavelength. However, lines marked * are at wavelengths longer than Littrow and are folded into the spectral region shown, overlapping lines in this region in some cases. The arrows around 515 nm indicate a baseline shift for the Ocean optics instrument. Lines in and around this region could not be measured with the Ocean Optics instrument. The rising baseline at wavelengths below 515 nm in the Ocean Optics spectra look like background light but this does not show up in the SHLS spectra.

The spectral range shown in Figures 3.6 and 3.7 is consistent with the theoretical value of ~30 nm (60 nm considering wavelengths above and below Littrow). This is a relatively small range for a general purpose LIBS spectrometer and could be an issue if the SHLS is used to measure LIBS spectra of a wide range of samples or to characterize unknown samples. Although the SHLS can be scanned to any spectral range, it would be more suitable for applications that do not require a large spectral range, such as monitoring a single element or close lying lines of a few elements, isotope measurements for elements with large isotope shifts, or for laser ablation molecular isotope spectrometry (LAMIS).

Figure 3.8 shows pulsed remote Raman spectra at 10 m using a 100-mm, f/1.25 Fresnel collection lens for the same minerals that were used for LIBS measurements along with the interferograms (inset). The Raman signal for the mineral samples was much lower than for sulfur or $KClO_4$, shown above using a CW laser. However, the background was also much lower than the LIBS spectra and also much lower than the CW remote Raman measurements. The use of a pulsed laser with a gated detector results in lower background for remote Raman and indicates that not all of the background is from Rayleigh scatter and at least some component must be from long lived luminescence, ambient light or detector noise, all of which would be reduced by gated detection. These data clearly show that remote Raman benefits greatly by the use of a gated detector. The spectral range shown is consistent with the theoretical value of 1073 cm^{-1} (30 nm) for a non-doubled SHRS using 150 gr/mm diffraction gratings. The interferograms are not symmetric, indicating uneven illumination in the SHS, possible a result of the relatively poor optical quality of the Fresnel collection optics. However, the Raman spectra are still obtained at a high SNR. Comparisons of the spectral quality of SHRS acquired Raman spectra, including remote measurements, have been previously published by our group,[4-6] as have remote Raman spectra of representative mineral samples.[15]

Figure 3.9 shows remote LIBS spectra at 10 m using a 100-mm, f/1.25 Fresnel collection lens (solid line spectra) of several hydrothermal vent solid samples that were acquired from four different deep ocean hydrothermal vent fields, including Tahi Moana, ABE, Tui Malila and Fenway. The inset shows an interferogram from the Tahi Moana sample. Independent analysis, supplied by Dr. Susan E. Humphris, Woods Hole Oceanographic Institution, of these samples showed 27% Ca, 5.5% Zn and 2% Fe for TH,

14% Ca, 11% Fe, 9% Cu for Fenway, 13% Zn, 30% Ba for TM and 7% Fe, 36% Zn and 4% Ba for the ABE samples. The same samples measured using an Ocean Optics LIBS spectrometer in a conventional non-remote mode are shown by the dashed line spectra. There is a baseline shift at ~515 nm in the Ocean Optics spectrometer and no useful emission can be measured in that region. A comparison of the Ocean Optics spectra shows similar lines above ~506 nm for the TH and Fenway samples, but the Ocean Optics spectrometer also shows lines below 506 nm for these samples. This shows the limited spectral range of the SHLS spectrometer below the Littrow wavelength (Littrow was set to 532 nm) of about 26 nm. The group of Ca I lines around 507 nm in the SHLS spectra (marked *) are strong Ca I lines above the Littrow wavelength that are folded into the spectral range plotted. The TM and AB samples show only strong Ba I lines in the wavelength range shown. These lines don't show up in the Ocean Optics spectra in this range because of the baseline shift.

3.5 CONCLUSIONS

A combined remote LIBS and Raman spatial heterodyne spectrometer is use to make measurements of a variety of samples at a distance of 10 m, using a ~100-mm diameter Fresnel lens as the collection optic. The results are compared to identical measurements made using a high quality ~100-mm aperture Questar long-range microscope. The overall quality of the spectra as indicated by fringe visibility in the interferograms is the same using each lens. However, spectral intensities are reduced by about a factor of 4 for the Fresnel lens, likely due to scattering and reflection losses as well as aberrations in the Fresnel optic. The results are encouraging, suggesting that Fresnel optics might be useful in applications where size and weight is restricted, such as in

instruments designed for spacecraft and planetary landers.

3.6 ACKNOWLEDGEMENTS

We would like to thank NASA [grant number NNX14AI34G] for funding this work. This work was also partially funded by the National Science Foundation [grant number CHE-1308211]. We thank Dr. Susan E. Humphris, Senior Scientist in the Geology & Geophysics Department, Woods Hole Oceanographic Institution, for supplying the hydrothermal vent samples and their analysis.

3.7 REFERENCES

1. J. M. Harlander, Spatial Heterodyne Spectroscopy: Interferometric Performance at Any Wavelength without Scanning. [Ph.D. Dissertation]. Madison, Wisconsin: University of Wisconsin-Madison, 1991.

2. J. M. Harlander, F. L. Roesler, R. J. Reynolds, K. Jaehnig, W. A. Sanders. "Differential, Field-Widened Spatial Heterodyne Spectrometer for Investigations at High Spectral Resolution of the Diffuse Far Ultraviolet 1548 Å Emission Line from the Interstellar Medium". Proc. SPIE. 1993. 2006: 139-148.

3. N. R. Gomer, C. M. Gordon, P. Lucey, S. K. Sharma, J. C. Carter, S. M. Angel. "Raman Spectroscopy Using a Spatial Heterodyne Spectrometer: Proof of Concept". Appl. Spectrosc. 2011. 65(8): 849–857.

4. N. Lamsal, S. M. Angel. "Deep-Ultraviolet Raman Measurements Using a Spatial Heterodyne Raman Spectrometer (SHRS)". Appl. Spectrosc. 2015. 69(5): 525–534.

5. N. Lamsal, S. M. Angel, S. K. Sharma, T. E. Acosta. "Visible and UV Standoff Raman Measurements in Ambient Light Conditions Using a Gated Spatial Heterodyne Raman Spectrometer". Paper presented at: LPSC 2015. Woodland TX; March 16-20.2015.

6. N. Lamsal, S. K. Sharma, T. E. Acosta, and S. Michael Angel, "Ultraviolet Stand-off Raman Measurements Using a Gated Spatial Heterodyne Raman Spectrometer," Appl. Spectrosc. 2016. 70(4): 666–675.

7. I. B. Gornushkin, B. W. Smith, U. Panne, N. Omenetto. "Laser-Induced Breakdown Spectroscopy Combined with Spatial Heterodyne Spectroscopy". Appl. Spectrosc. 2014. 68(9): 1076-1084.

8. National Academies of Sciences, Engineering, and Medicine. 2011. Visions into Voyages for Planetary Sciences in the Decade 2013-2022. Washington, DC: The National Academies Press.

9. What are SmallSats and CubeSats? http://www.nasa.gov/content/what-are-smallsats-and-cubesats. 2016.

10. Barnett, Patrick D. and Angel, S. Michael "Miniature Spatial Heterodyne Raman Spectrometer with a Cell Phone Camera Detector". Appl Spectrosc. 2016. 71(5): 988-995.

11. Barnett, Patrick D. "The Development of a Miniature Spatial Heterodyne Raman Spectrometer for Applications in Planetary Exploration and Other Extreme Environments," [Ph.D. Dissertation]. Columbia, South Carolina: University of South Carolina, 2016.

12. Mini DPSS pulsed laser sources for LIBS are available: http://bwtek.com/products/sub-ns-dpss-pulse-laser-oem-module/.

13. Yeh, Naichia "Analysis of spectrum distribution and optical losses under Fresnel lenses." Renewable and Sustainable Energy Reviews. 2010. 14(9): 2926-2935.

14. J. M. Harlander, F. L. Roesler, S. Chakrabarti. "Spatial Heterodyne Spectroscopy: A Novel Interferometric Technique for the FUV". In: O. H. W. Siegmund; H. S. Hudson, editors. EUV, X-Ray, and Gamma-Ray Instrumentation for Astronomy. Proc. SPIE. 1990. 1344: 120-131.

15. M. J. Egan, S. M. Angel and S. K. Sharma. "Standoff spatial heterodyne Raman spectrometer for mineralogical analysis". J. Raman Spectrosc. 2017. 48: 1613–1617.

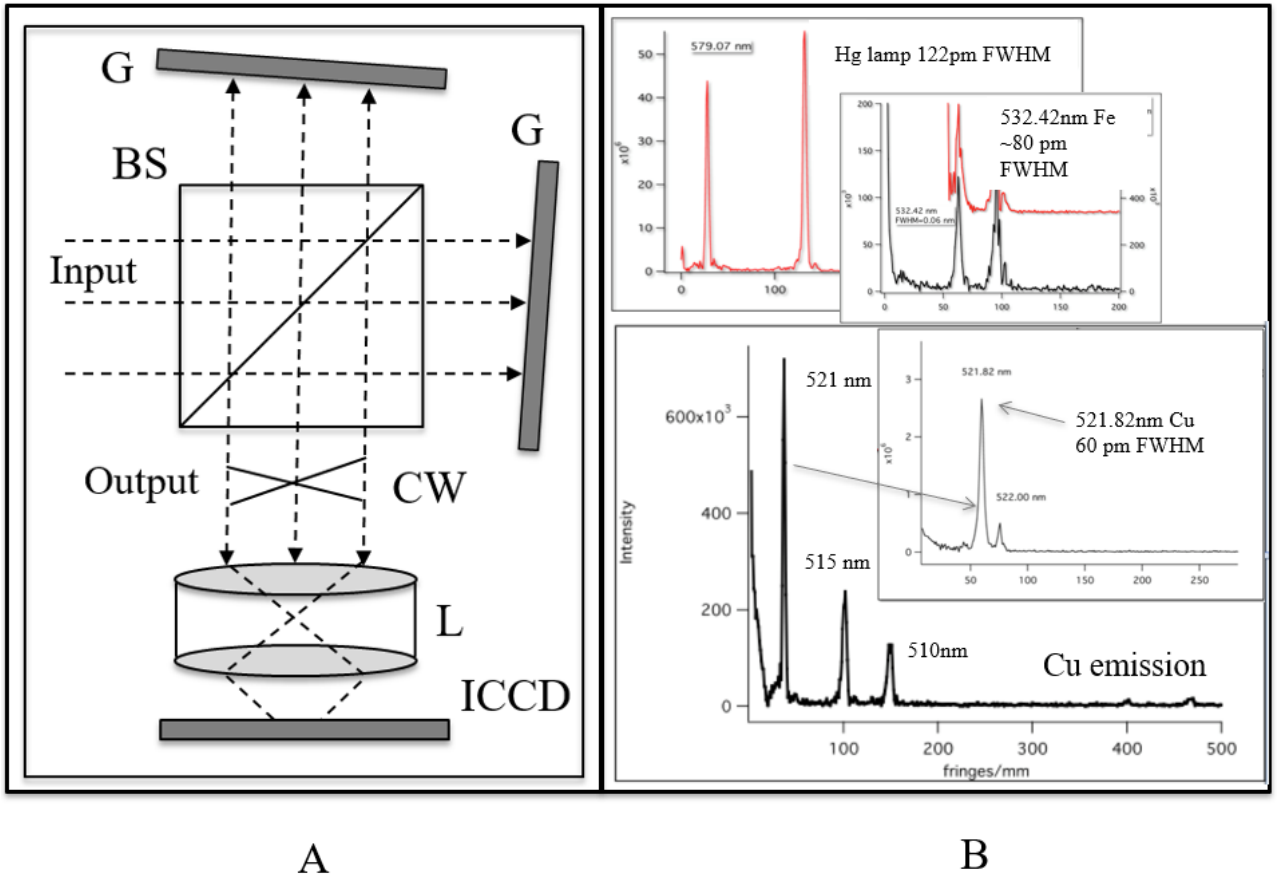

Figure 3.1. (A) Spatial heterodyne spectrometer (SHS). BS=beam splitter, G=diffraction grating, CW=crossing wavefronts, L=lens, ICCD=intensified charge coupled device detector. (B) For an SHS using 600 g/mm diffraction gratings, the spectral resolution is shown for spectral lines of a Hg emission lamp and two LIBS spectra of Fe and Cu. The measured resolution for these lines is 112pm, 80pm, and 60pm for Hg, iron and Cu, respectively.

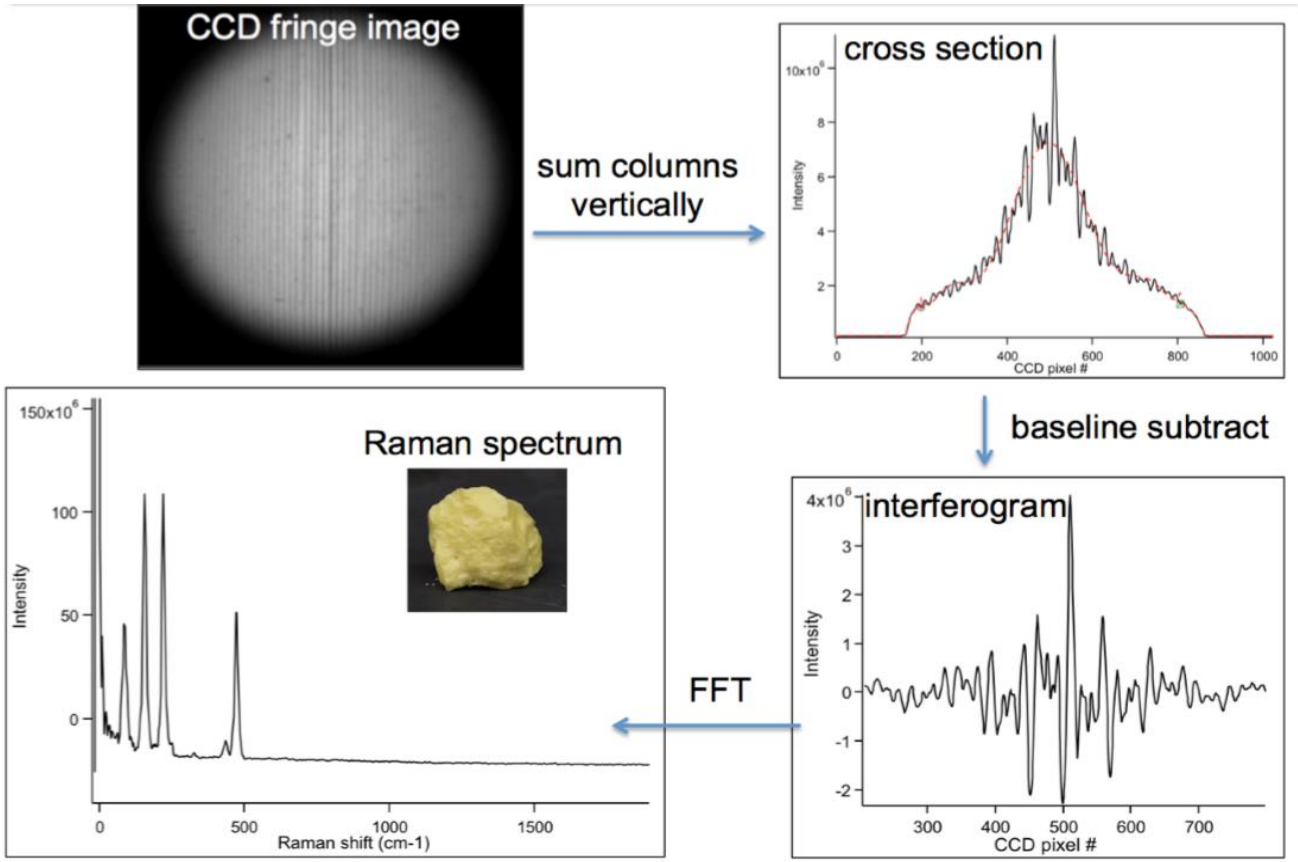

Figure 3.2. This shows how spectra are recovered from the SHS fringe images. The signal is collected and measured as a fringe image on the detector (upper left). The columns of the image are summed in the vertical direction to provide a raw interferogram superimposed on a dc background signal (upper right). The ac component of the interferogram is obtained by subtracting the background, usually by fitting a high order polynomial (lower right), and the Raman or emission spectrum is obtained by taking the 1D Fourier transform of the interferogram (lower left).

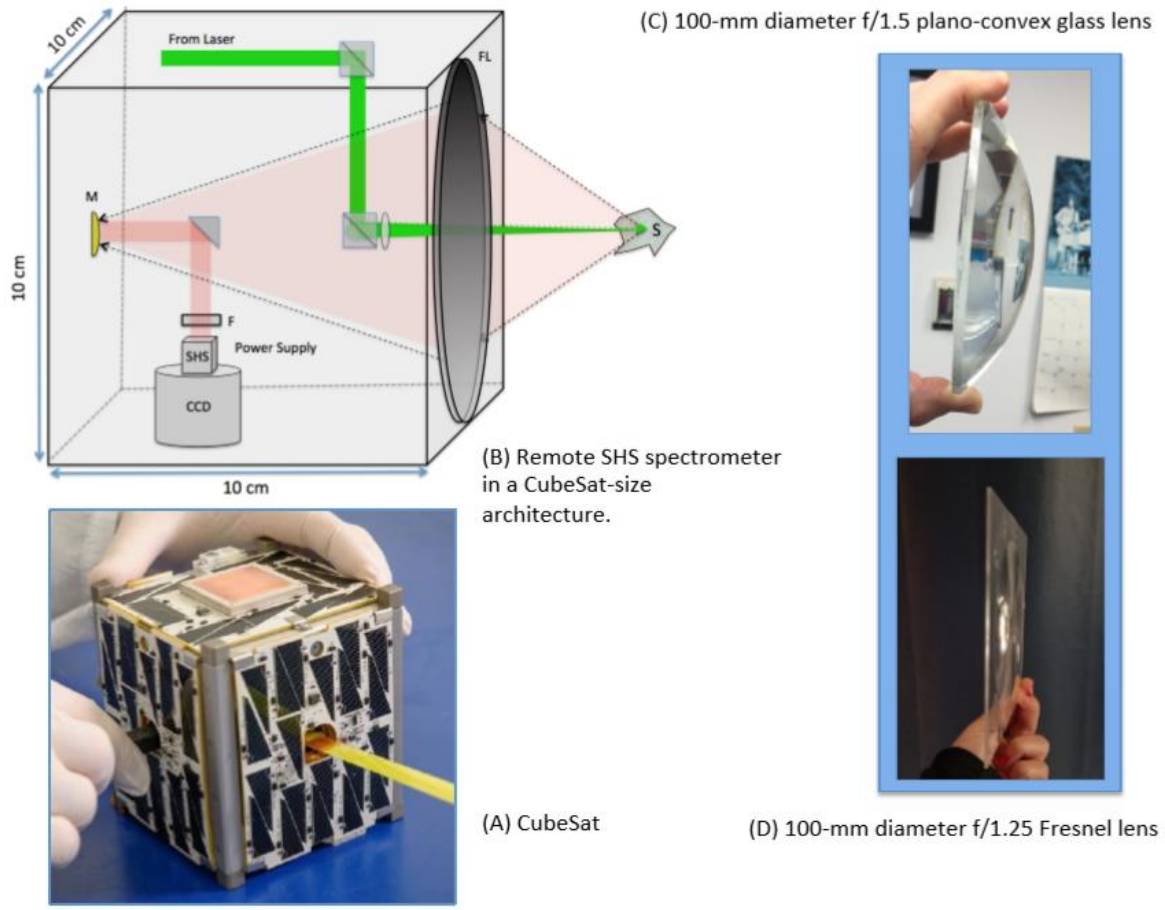

Figure 3.3. (A) A picture of a CubeSat developed by NASA. (B) Shows how a fast collection lens as large as ~10 cm and a small SHS spectrometer can both be included in a 1U CubeSat architecture. To fit the 1U architecture, the collection optic must be ~f/1. Although large f/1 glass or quartz lenses and mirrors are available, they are typically very thick and heavy as shown by the f/1.5 lens in (C). The Fresnel lens is much thinner and lighter as shown in (D).

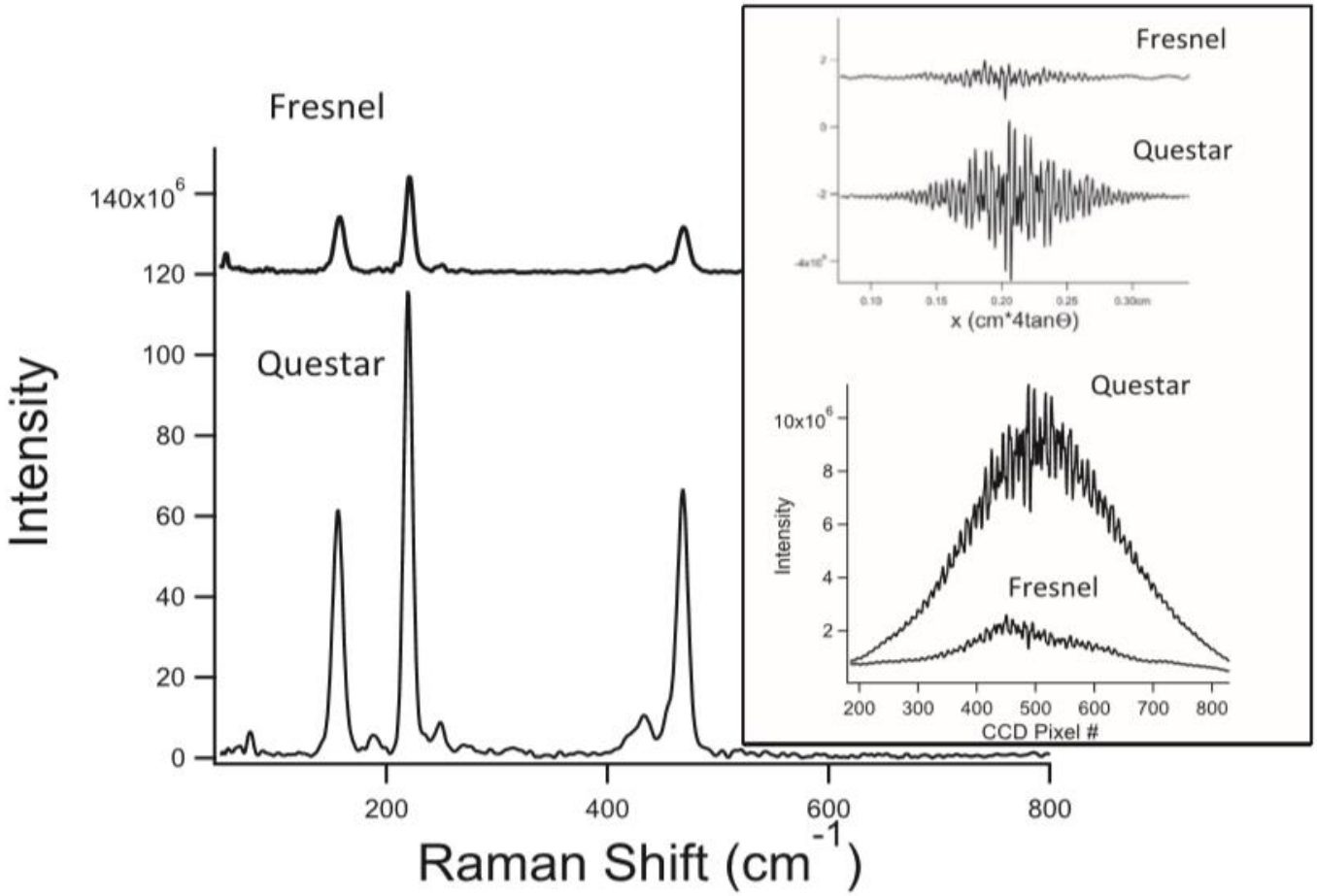

Figure 3.4. Sulfur remote Raman spectra at 10 m using the CW 532 nm laser, 5 s integration time, and using two different collection optics, a simple 100-mm diameter f/1.25 Fresnel lens (top) and a 100-mm aperture Questar long distance microscope (lower). Lower inset: raw interferograms. Upper inset: background subtracted interferograms.

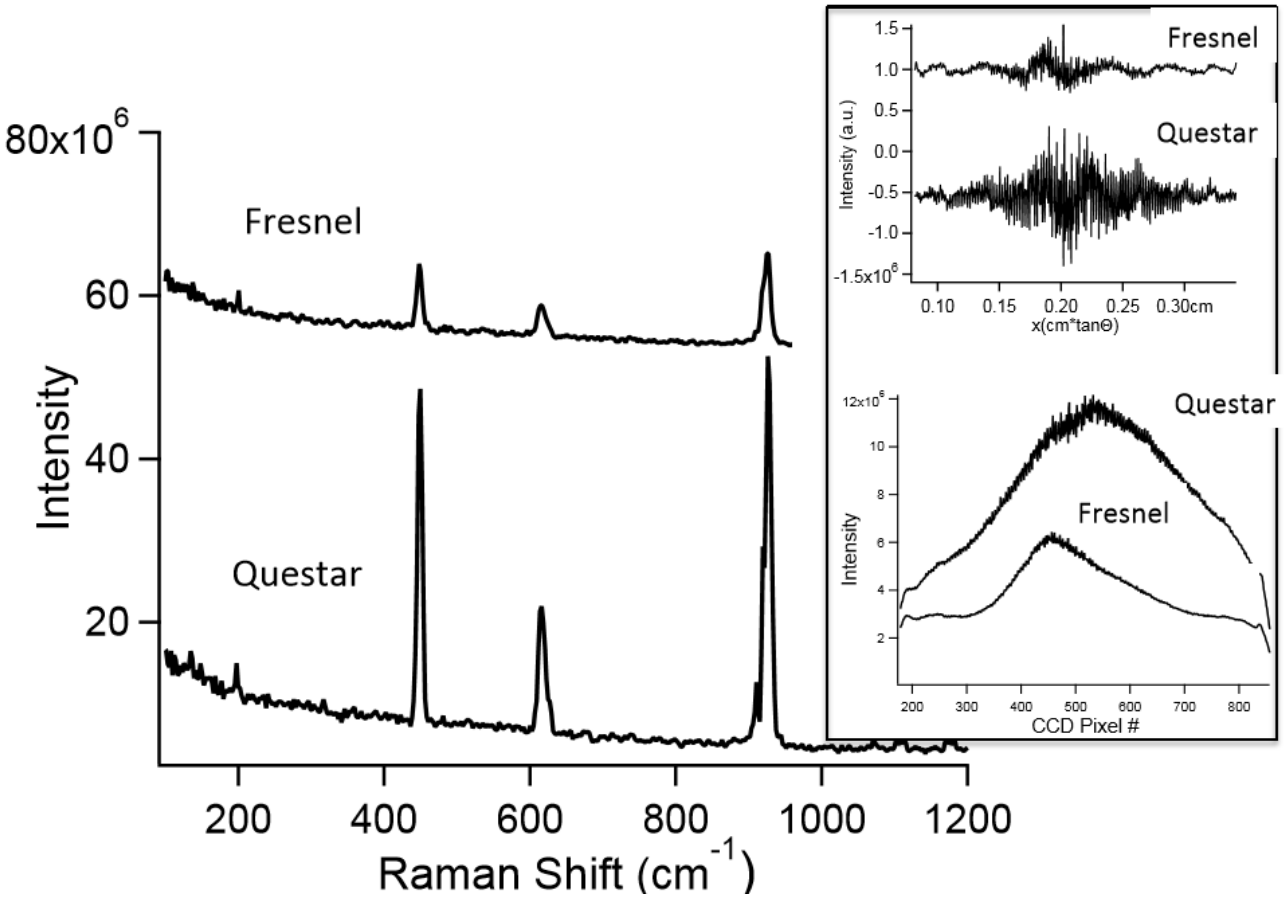

Figure 3.5. $KClO_4$ remote Raman spectra at 10 m using the CW 532 nm laser and 60 s integration time collected with a Fresnel lens (top) and the Questar long distance microscope (lower) for collection. Lower inset: raw interferograms. Upper inset: background subtracted interferograms.

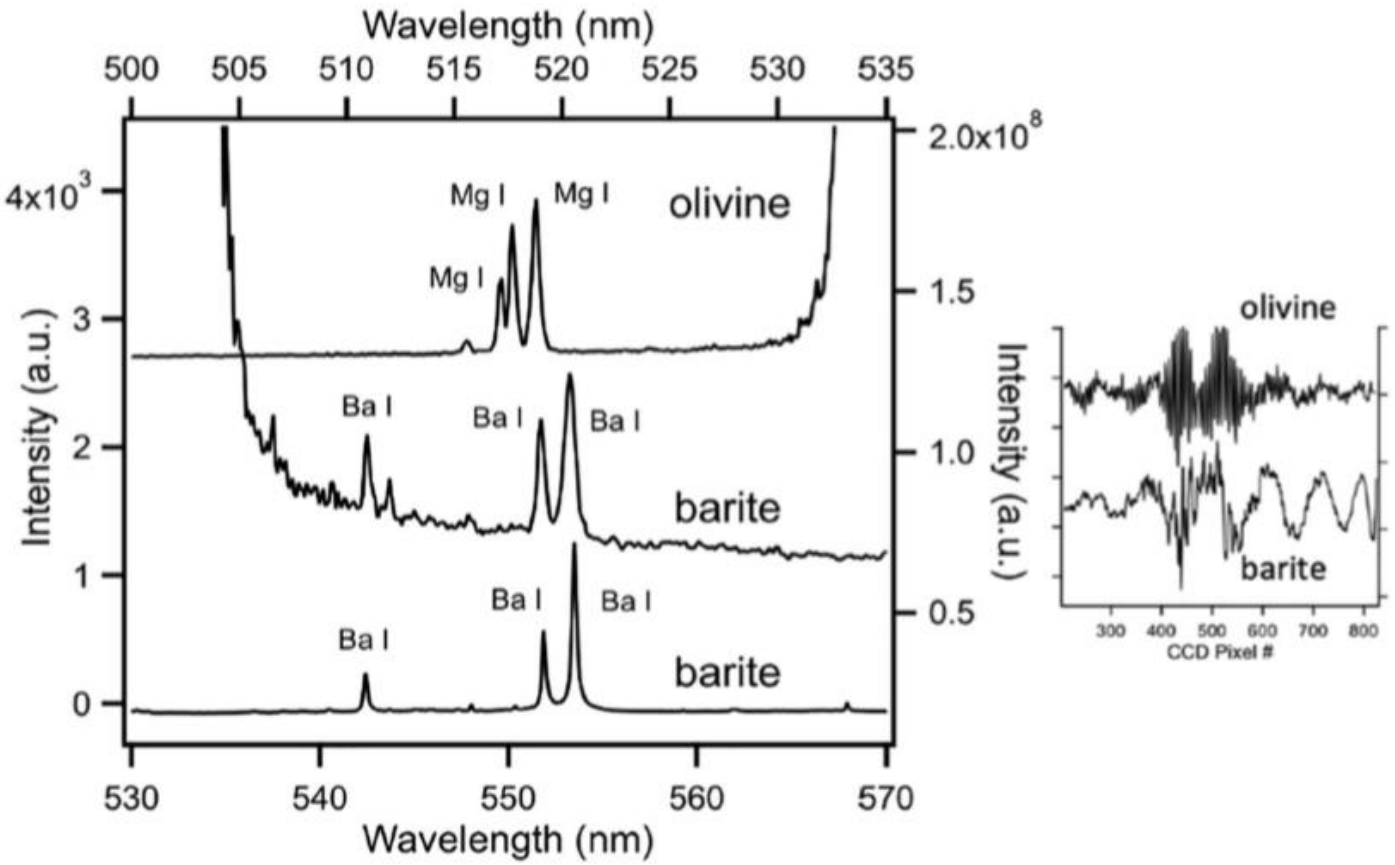

Figure 3.6. Remote SHS LIBS spectra using the pulsed 532 nm laser with a gated detector using a 100-mm, f/1.25 Fresnel collection lens of two mineral samples, olivine (top spectrum, upper wavelength scale) and barite (middle spectrum, lower wavelength scale) at 10m using the Fresnel lens. Spectra are recorded using 100 laser shots, 2.3 us gate delay, 2 us gate width, and 124.5mJ 532nm excitation. The bottom barite LIBS spectrum was measured using a pulsed 1064nm laser and recorded with a conventional LIBS spectrometer, LIBS-2000+ by Ocean Optics. Right: SHS interferograms for barite (lower) and olivine (upper).

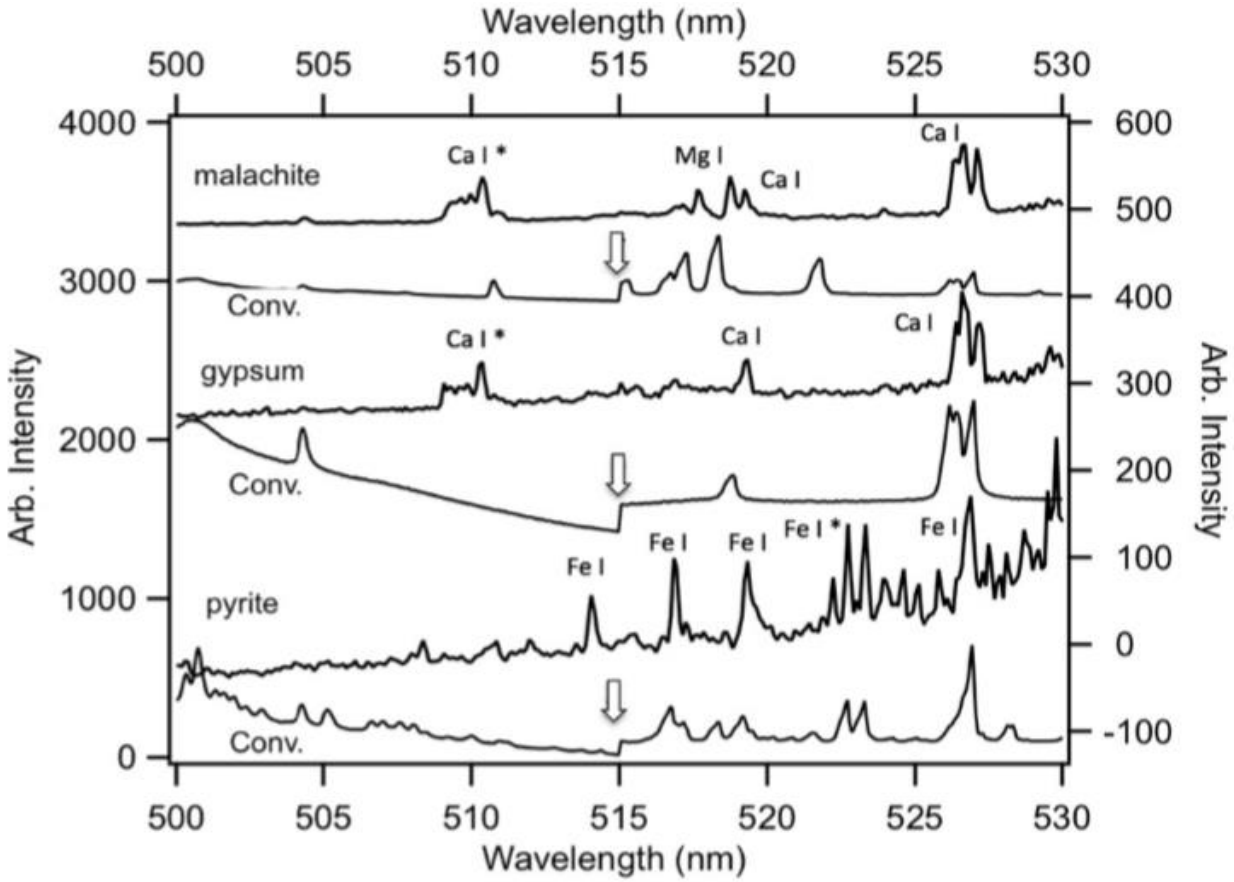

Figure 3.7. Remote LIBS spectra using the pulsed 532 nm laser with a gated detector of the minerals malachite, gypsum and pyrite at 10m using a 100-mm, f/1.25 Fresnel collection lens. SHS spectra are recorded using 100 laser shots, 2.3 us gate delay, 2 us gate width, and 124.5 mJ 532 nm excitation. Below each SHS spectrum is the corresponding spectrum (Conv.) that was measured using a pulsed 1064 nm laser and recorded with a conventional LIBS spectrometer, LIBS-2000+ by Ocean Optics. *Lines above Littrow.

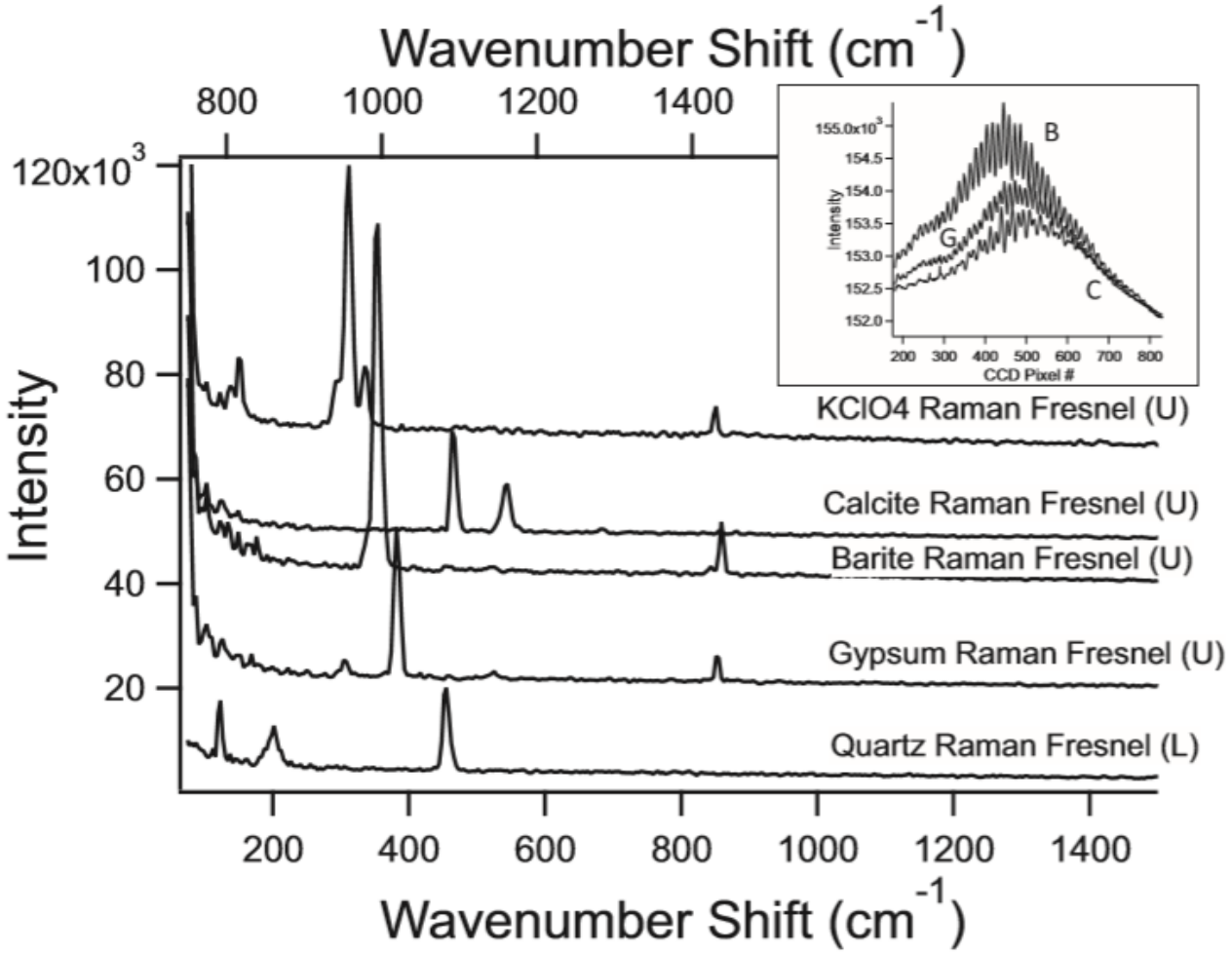

Figure 3.8. Remote pulsed SHS Raman spectra of mineral samples at 10 m using a 100-mm, f/1.25 Fresnel collection lens. 100 ns gate delay, 1 us gate width, 500 shots at 5Hz using 24.9 mJ 532 nm. Inset: interferograms (not background subtracted) for barite (B), gypsum (G) and calcite (C).

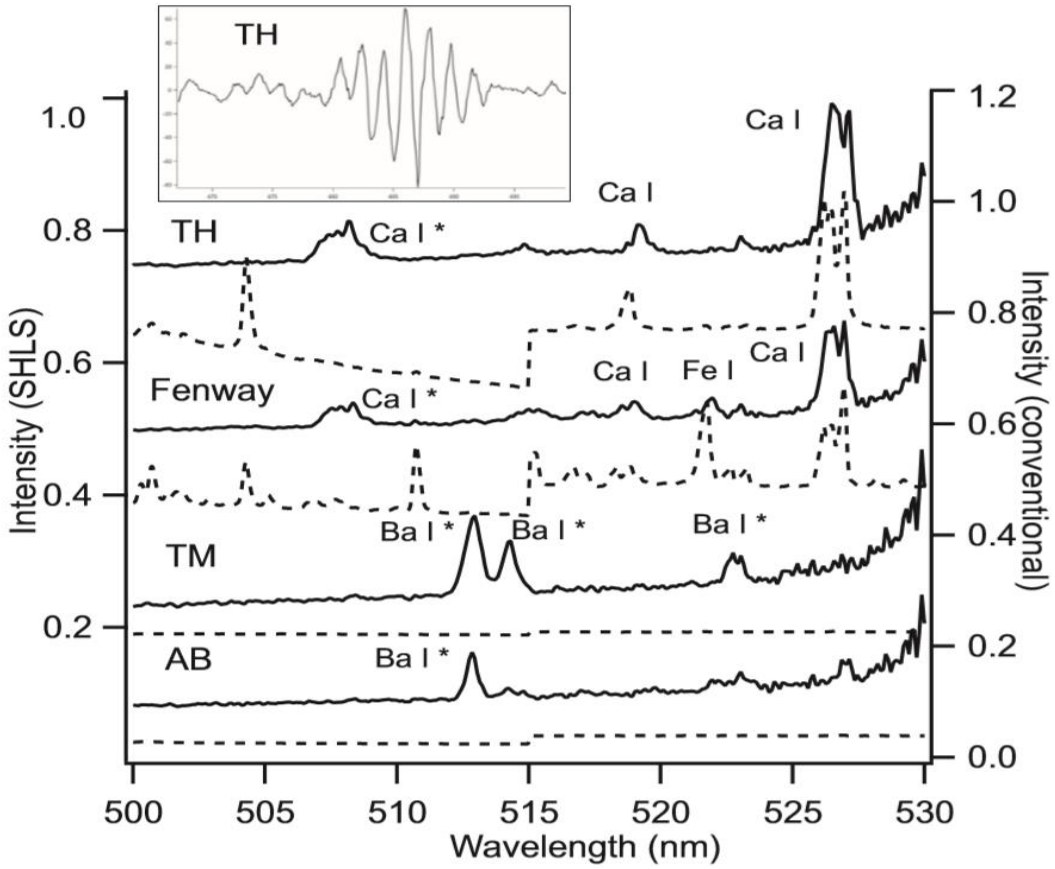

Figure 3.9. Solid line spectra: Remote SHS LIBS spectra of several solid hydrothermal vent samples at 10 m distance using the pulsed 532 nm laser with a gated detector and a 100-mm, f/1.25 Fresnel collection lens. The four samples come from hydrothermal vent fields, Tahi Moana (TH), ABE (AB), Tui Malila (TM) and Fenway. The inset shows one interferogram for the TH sample. Note: * indicates emission lines above Littrow. Dashed line spectra: The same samples measured using an Ocean optics LIBS spectrometer in a conventional sample setup, non-remote, mode. Note: the baseline shift at ~515 nm is a feature of the Ocean Optics spectrometer and no useful emission can be measured in this region.

CHAPTER 4

HYPERSPECTRAL RAMAN IMAGING USING A SPATIAL HETERODYNE RAMAN SPECTROMETER WITH A MICROLENS ARRAY[B]

[B]Allen, A., Waldron, A., Ottoway, J., Carter, J. C. and Angel, S. M. 2019. Submitted to *Applied Spectroscopy*. 10/10/2019.

4.1 ABSTRACT

A new hyperspectral Raman imaging technique is described, using a spatial heterodyne Raman spectrometer (SHRS) and a microlens array (MLA). The new technique allows Raman spectra over a wide spectral range to be acquired in two spatial dimensions (x, y) using a single exposure on a charge coupled device (CCD) or complementary metal-oxide semiconductor (CMOS) detector. In the SHRS system described here, a 4x4 mm MLA with 1600, 100 µm diameter lenslets is used to image the sample, with each lenslet illuminating a different region of the SHRS diffraction gratings, and forming independent fringe images on the CCD. The fringe images from each lenslet contain the fully encoded Raman spectrum of the region of the sample "seen" by the lenslet. Since the SHRS requires no moving parts, all fringe images can be measured simultaneously with a single detector exposure, and in principle using a single laser shot, in the case of a pulsed laser. In this proof of concept paper, hyperspectral Raman spectra of a wide variety of heterogeneous samples are used to characterize the technique in terms of spatial and spectral resolution tradeoffs. It is shown that the spatial resolution is a function of the diameter of the MLA lenslets, while the number of spatial elements that can be resolved is equal to the number of MLA lenslets that can be imaged onto the SHRS detector. The spectral resolution depends on the spatial resolution desired, and the number of grooves illuminated on both diffraction gratings by each lenslet, or combination of lenslets in cases where they are grouped.

4.2 INTRODUCTION

The spatial heterodyne Raman spectrometer (SHRS) is a fixed grating, Fourier transform interferometer with high light throughput, a wide field of view (FOV), and high

spectral resolution. Unlike conventional, dispersive grating-based spectrometers, the resolving power of the SHRS is not strongly dependent upon entrance aperture size. The SHRS also has no moving parts, and SHS emission spectrometers have been built using monolithic optical techniques, which makes the system robust and tolerant of vibrations.[1] Lastly, the large acceptance angle of the SHRS makes it amenable to applications involving the collection of light from diffuse sources, or for remote Raman where image jitter can affect the reproducibility using a slit-based spectrometer.[2] Applications like remote Raman, transmission Raman, spatially offset Raman and Raman imaging may benefit from the larger viewing area of the SHRS. This paper describes an innovative way to perform two-dimensional (2D) Raman chemical imaging using the SHRS, which takes advantage of the large viewing area of the SHS.

Raman imaging is useful to characterize heterogeneous materials by measuring chemical properties in multiple spatial dimensions.[3] A Raman image can be 2D, where the intensity of a single Raman band is mapped across the heterogenous sample, or hyperspectral, where multiple Raman band intensities are acquired for each spatial point on the sample. Early Raman microprobes were scanning instruments, where the laser mapped the sample surface to generate the hypercube of data, either point-by-point or by line scanning the laser across the sample.[4] For point-by-point scanning, the laser is focused to a small spot and the sample is raster scanned through the laser beam, collecting the entire Raman spectrum at each point.[5] In line scanning, the laser is focused to a thin line, using cylindrical optics. The illumination line on the sample is parallel to the entrance slit of a dispersive spectrometer so that a Raman spectrum is acquired on each row of a two-dimensional array detector.[6] Wide field Raman imaging measures all points on the sample

simultaneously using an expanded laser spot while a single Raman band is measured using a tunable filter to acquire a 2D Raman image. The hyperspectral image is built up by measuring Raman images as the filter is tuned to different Raman bands. Various types of filters have been used in this method, including dielectric filters, acoustooptic and liquid crystal tunable filters.[7-15] Fiber optic arrays have been used for hyperspectral Raman imaging, where spatial and spectral information were simultaneously acquired. However, the number of spatial points demonstrated using a fiber array is low and the fiber fill factor is also low.[16]

Here we describe a new hyperspectral Raman imaging technique using a microlens array (MLA) in a confocal imaging arrangement with a spatial heterodyne Raman spectrometer. The MLA is an array of microlenses, with diameters ranging from 10 microns to 2 mm, where each views a different spot on the sample. The use of MLA's for confocal microscopy has been described previously; Dwight et. al. reports fluorescence microscopy using an MLA with a prism to collect fluorescence data with ~20 nm spectral resolution.[17] This technique has not previously been applied to Raman. The MLA-SHRS instrument described in this paper allows the measurement of a hyperspectral Raman image, covering the entire Raman fingerprint range (e.g., ~2500 cm^{-1}), in a single measurement. In this proof of concept paper, Raman fringe images with up to up to ~550 spatial points are demonstrated, and our data indicates that many thousands of points (e.g., ~10,000) can be simultaneously imaged while maintaining a large spectral range, in an optimized instrument.

4.3 EXPERIMENTAL

4.3.1 ILLUMINATION

The sample was excited by a continuous wave (CW) 532 nm Nd:YAG laser (OptoEngine, MLL-FN-532-300mW) in an epi-illumination backscatter geometry. The laser beam diameter was 2.2 mm. The laser was directed to the sample on the axis of the SHRS spectrometer, using a 25 mm diameter, 550 nm long pass dichroic mirror (ThorLabs, DMLP550), and was focused on the sample by the microlens array (MLA) (Suss MicroOptics, part no. 19-0055), with each lenslet focusing the laser to a separate small spot, with an airy disk of ~20 micron, to give an array of 484 laser spots on the sample. The laser power focused by each separate lenslet was ~300 μW at the sample. The sample was located at the focal point of the f/16 MLA, a distance of 1.5 mm. The fused silica MLA is 4x4 mm overall size with 1600, 100 micron diameter circular lenslets, packed in a square grid, with a fill factor close to 80%. The MLA has Chromium apertures that block light between the lenslets to prevent crosstalk, and it is antireflection coated at 780 nm. The flat surface was turned opposite the sample, in the direction of the spectrometer.

4.3.2 LIGHT COLLECTION

Raman scattered light from the sample was collected by the MLA and collimated, each lenslet having a unique spatially isolated field of view on the sample (FOV) from the others, producing its own separate collimated beam. A relay lens (Nikon AF NIKKOR 80-200 mm f/4.5-5.6), was used to image the back surface of the MLA onto the SHRS gratings. The distance used depended on the desired magnification, 4X, 8X or 10X, of the MLA at the SHRS gratings. The magnification was used to change the number of lenslets measured and the resolving power for single lenslets. A 4 mm diameter spatial filter,

located at the focal point of the relay lens, minimized crosstalk between lenslets, as described by Tiziani et al.[18,19]

4.3.3 SPATIAL HETERODYNE SPECTROMETER

The SHRS, similar to ones described previously, is equipped with a 25 mm N-BK7 non-polarizing 50:50 cube beamsplitter (ThorLabs, BS013) and a pair of 300 lp/mm gratings, blazed at 500 nm (Edmund Optics, #64-403).[20,21] An iris at the input aperture limits the size of the illuminated area on the gratings to ~14 mm. The SHRS was equipped with two 532 nm long pass filters (Semrock RazorEdge, LP03-532RE-25), a 550 nm long pass filter (ThorLabs, FEL0550) and a 581 nm short pass filter (Knight Optical, 581FDS25) to remove strong laser scatter, and to limit the total spectral range (bandpass) allowed into the spectrometer. A fused silica 105 mm focal length, f/4.5 lens (Coastal Optical Systems, Inc., UV-MICRO-APO 111032) imaged the grating faces to produce the fringe image with 1.17X magnification onto a thermoelectrically-cooled back-illuminated UV-enhanced CCD detector with 2048 x 512, 13.5 µm pixels (Princeton Instruments, PIXIS-2048 2KBUV). A spatial filter placed one focal length behind the imaging lens was used to block higher grating orders. Images were acquired in Lightfield 4.10 software with 100kHz ADC gain high and in the low noise setting. The CCD was cooled to -70^{o} C. For the Raman image in Fig. 8, a CMOS detector with 5544 x 3694, 2.4 µm pixels was used (QHYCCD, QHY183M).

4.3.4 SPECTRAL CALCULATIONS, FFT

All spectral calculations were done using MATLAB (MathWorks, version R2016a) To obtain Raman spectra from the fringe images, a region of interest is selected and the rows are summed, in the vertical direction, to give an interferogram superimposed on a

background signal, and the background is removed by subtracting a fitted polynomial curve. The corrected interferogram is then Fourier transformed using the MATLAB FFT function, to reveal the Raman spectrum, plotted as magnitude versus wavenumber. For 2D SHRS measurements, one grating was slightly tilted from the vertical to produce a wavenumber dependent fringe rotation that reduces the ambiguity of bands above and below the Littrow wavenumber.

4.3.5 SAMPLE PREPARATION

Several bilayer mixed sample pellets were prepared using a 13 mm pellet die (Carver, catalog #3619). Samples were prepared with the intention of keeping the constituents spatially separated so that different samples were viewed by different lenslets of the MLA. The samples included a diamond (Wards Science, kit #458200) pressed into a potassium perchlorate (Alfa Aesar #11630, 99% anhydrous) pellet, a sodium sulfate (Sigma Aldrich, 239313)/potassium perchlorate pellet, a sodium nitrate (Sigma Aldrich, 347663)/potassium perchlorate pellet, and an acetaminophen (Sigma-Aldrich, A7085)/ammonium nitrate (Aldrich, 256064) pellet.

4.4 RESULTS AND DISCUSSION

The SHRS is a dispersive interferometer that uses two stationary reflective diffraction gratings. Operation of the SHRS has been described previously.[20-22] Briefly, collimated signal enters the input aperture of the SHRS where it is split into two beams by a 50:50 beamsplitter. These two beams strike the stationary diffraction gratings which are tilted at an angle, θ_L, such that one particular wavelength, the Littrow wavelength, λ_L, is retro-reflected along the incident light path and recombines at the beamsplitter. Heterodyning in the interferometer occurs at the Littrow wavelength, so light at

wavelengths longer or shorter than λ_L are diffracted from the gratings at an angle to the optical axis, resulting in crossed wavefronts, inducing a spatial phase shift, and generating an interference pattern, which produces a series of wavelength dependent vertical fringes on the array detector. The intensity of the fringe pattern is a function of position x on the detector, given by Eq. 4.1.

$$I(x) = \int B(\sigma)\{1+\cos[8\pi\,(\sigma-\sigma_L)x\,\tan\theta_L]\}d\sigma \qquad \text{Eq. 4.1}$$

$B(\sigma)$ is the input spectral intensity at wavenumber σ, and the Fourier transform (FT) of $I(x)$ recovers the Raman spectrum. The fringe frequency on the detector is given by Equation 4.2, where f is in fringes/cm, σ_L is the Littrow wavenumber and σ is the wavenumber of interest.[22]

$$f = 4(\sigma - \sigma_L)\tan\theta_L \qquad \text{Eq. 4.2}$$

According to Equation 4.2, emission lines above or below the Littrow wavelength show identical fringe patterns, leading to degenerate lines (i.e., line overlap). This degeneracy can be removed by tilting one of the gratings vertically or rotating it about the optical axis, which induces a rotation to the fringes, in opposite directions above and below Littrow.[21,22] In this case, a two-dimensional (2D) Fourier transform can be used to recover spectra above and below the Littrow wavelength, unambiguously. This is very useful to double the spectral range of the SHRS.

The SHRS, like other Fourier transform interferometers, does not require a slit to control the spectral resolution, as in dispersive spectrometers. The resolving power of the SHRS is proportional to the total number of grooves illuminated on both gratings. This allows the SHRS to employ large entrance apertures, greatly increasing the throughput of the system, which is advantageous for measuring extended sources, such as when a large

laser spot might be used to reduce sample damage, a large diameter optical fiber is used to deliver light to the spectrometer, or other applications where large sample areas need to be measured, such as the imaging technique described in this paper.

In the SHRS used for these studies (see Fig. 4.1A), the width of the input beam at the gratings is ~14 mm, so the theoretical resolving power, *R*, is 8,400, giving a theoretical resolution of ~2 cm^{-1} for a 1000 cm^{-1} Raman band, using 532 nm excitation. This spectral resolution is about the same as a Kaiser Holospec f/1.8 spectrometer, with a 25 μm slit.[23] The measured spectral resolution of the SHRS was ~7 cm^{-1}, using a low-pressure Hg lamp source (Ocean Optics, Hg-1). The measured resolution of the SHRS is very sensitive to alignment of focusing optics, likely the cause for the lower the expected resolution.

The illuminated width of the CCD is 14.8 mm, ~1100 pixels, so the theoretical spectral range of the SHRS, based on the Nyguist criteria of 2 pixels per wavelength, is ~1155 cm^{-1}. The spectral range can be doubled to ~2310 cm^{-1} using the 2D Fourier transform technique described above. The throughput of the SHS is larger than a conventional dispersive spectrometer of comparable spectral resolution, from the combination of a large aperture and wide FOV. The maximum, resolution-limited solid angle FOV of the SHRS is related to the resolving power by Equation 4.3.[22] The solid angle FOV for the spectrometer used in the studies presented here is 7.5 x 10^{-4} sr, corresponding to a full acceptance angle of ~1.6°.

$$\Omega_{max} = 2\pi/R \qquad \text{Eq. 4.3}$$

Figure 4.2A shows how the MLA is imaged onto the face of the gratings by the relay lens. The 40x40 MLA used in this work is shown in Fig. 4.2B. Light from each lenslet of the MLA takes a unique path through the interferometer, each providing its own

independent fringe image. In Fig. 4.2A, the light path for two lenslets is illustrated. Each of the 1600 MLA lenslets has the same focal length, and the sample is placed one focal length from the MLA. The laser is focused by each MLA lenslet to a small spot on the sample. Scattered Raman light is collected by the MLA lenslets to produce an array of collimated beams, one for each lenslet. The relay lens is positioned to image the back surface of the MLA onto the SHRS gratings. A spatial filter, located at the focal point of the relay lens, prevents crosstalk between the field of view of MLA lenslets, as described by Tiziani et. al.[18,19] Figure 4.2C shows the Raman image for the sulfur pellet, shown in Fig. 4.2D, measured with the MLA-SHRS, and shows almost all of the 1600 MLA lenslets (notice the ridge detail of the sulfur pellet that is retained in the MLA-SHRS image). However, with the CCD used for this work, individual lenslet fringes could not be resolved. This is a limitation of the number of pixels on our detector; in this case only providing 8 pixels per lenslet, not sufficient to resolve fringes. Resolving all 1600 lenslet fringe images would require a CCD with much smaller pixels.

Figure 4.1B shows Raman spectra measured using the MLA-SHRS system shown in Fig. 4.2. The detector images, shown with each spectrum, show the individual lenslets that are viewed and the position of each sample within the FOV. The samples consisted of a series of bilayer pellets, that were illuminated at the interface between the two constituents, so that both solids were within the FOV of the instrument. The imaged area shown was about 12 lenslets wide by about 5 lenslets tall, giving a measured sample area of 1.32 mm x 0.55 mm. The number of lenslets viewed was limited by the spectral resolution of the grating used in these studies—these limitations are discussed in a later section. For the spectra shown, the MLA was not used for imaging, rather, the signal from

all lenslets were summed to produce the spectrum, so they represent the mean Raman spectra over the total area measured. The measured resolution was ~7 cm^{-1} for the potassium perchlorate/diamond and sodium sulfate/potassium perchlorate samples. The resolution was slightly lower, ~8-9 cm^{-1}, for the sodium nitrate/potassium perchlorate and an acetaminophen/ammonium nitrate pellets, because the imaging magnification was slightly larger (8X) than in the former (10X). The spectral range for these spectra is ~1150 cm^{-1}, consistent with the theoretical value. Raman spectra using fringe images from the individual lenslets, for each of the samples shown in Fig. 1B are described in the following.

Figure 4.3 shows how MLA-SHRS lenslet spectra are recovered for a diamond sample. The signal is collected and shown as an array of fringe images (upper left image), one from each lenslet, on the detector. The fringe image cross section (upper right), produced by summing pixels vertically in each column, for a selected lenslet fringe image, (shown by white box), shows an interferogram superimposed on a large background signal. The background is removed by subtracting a fitted a polynomial from the cross section. The spectrum is obtained by taking the 1D Fourier transform of the resulting interferogram. The resulting diamond Raman spectrum has a spectral resolution of ~41 cm^{-1}, lower than the 6 cm^{-1} achieved for the diamond sample shown in Fig. 4.1B (i), because of the lower number of grooves illuminated by a single lenslet on the grating.

The 2D spectral range doubling technique can be applied to double the spectral range for each lenslet spectrum. Figure 4.4 shows a 2D interferogram for an acetaminophen sample (left), cropped to show clearly the crossed fringe pattern, for a 4 x 4 section of lenslets. The Littrow wavenumber of the SHRS was set to ~1000 cm^{-1}, indicated by σ_L in the spectra, so Raman bands above and below Littrow rotate the fringes

in opposite directions. Raman spectra (right) for the regions A-C, labeled on the detector fringe image were obtained via a 2D Fourier transform. Using the MLA-SHRS for Raman imaging, there is a tradeoff between spectral resolution and number of lenslets used in the horizontal direction (e.g., grating grooves illuminated). For example, the spectra produced by region A for a single lenslet, and region B which covers four lenslets vertically, produce spectra with the same resolution, ~42 cm^{-1}, because both regions illuminate the same number of grating grooves. However, the spectrum produced by region C, viewing 4 lenslets horizontally, has four times higher resolution, ~11 cm^{-1}, because 4 times as many grating grooves were illuminated. The intensity scales with the number of lenslets viewed, regardless of the direction.

Figure 4.5 shows the Raman image (top left) for a diamond/perchlorate sample (top right). In this image, the MLA was magnified by 10X onto the gratings, and 60 different lenslets are shown, corresponding to a sampled area on the sample of 1.32 x 0.55 mm^2. Lenslets outside this area didn't show high contrast fringes. The image is brighter in the diamond region because the diamond Raman cross section is ~3.8 times larger than perchlorate.[24,25] Spectra corresponding to three different sample regions are shown (bottom left). Region A shows only the diamond Raman band at 1332 cm^{-1}, region B shows both potassium perchlorate and diamond Raman bands, and region C shows only the 941 cm^{-1} Raman band of potassium perchlorate.[26,27]

The size of the image of each lenslet on the gratings is 0.98 mm. For the 300 lp/mm gratings, this corresponds to a theoretical resolving power of 588, which gives a theoretical spectral resolution of 32 cm^{-1}. The measured resolution of the spectra shown in Fig. 5 are consistent with this value, at 33 cm^{-1}. The grating image is magnified 1.17X on the CCD,

so each lenslet has a diameter of 85 pixels, thus allowing 85/2 spectral elements to be measured, giving a theoretical spectral range of 1,360 cm^{-1}. The observed one-lenslet spectral range, ~1,250 cm^{-1}, is consistent with this value.

The Raman image in Fig. 4.6 (top left), measured in the same configuration as in Fig. 4.5, shows an example of resolving close lying Raman bands for two samples, sodium sulfate/potassium chlorate, that are separated by no more than two lenslet diameters. The interface between the samples, labeled in the picture inset with a dashed line, is not immediately obvious in the white light image, because both constituents have similar Raman scattering cross sections.[25] The measured spectral resolution for the Raman spectra (bottom left) of the three lenslet regions (A, B and C) is ~33 cm^{-1}, adequate to distinguish between the sodium sulfate band at 990 cm^{-1} and potassium perchlorate Raman band at 941cm^{-1}. Note, in this case, the brightness of the lenslets in the Raman image is not indicative of the sample type because in these images we did not correct for changes in light intensity across the image, as might occur from such things as changes in laser power, sample position or flatness with respect to the MLA image plane, density variations in the sample, sample refractive index differences, or luminescence impurities in the samples.

For transparent, highly scattering samples, the spatial resolution of any Raman imaging technique is limited by diffuse scattering of the laser through the sample, so the laser is not localized at the focal point of the laser but can excite Raman scattering up to many mm away. Spatially offset Raman takes advantage of this effect, to increase the volume that is probed for highly scattering samples such as pharmaceutical tablets.[14] This is illustrated by the Raman image in Figure 4.7, for a sodium nitrate/potassium perchlorate sample (top right). In this image, showing Raman from 60 different MLA lenslets,

covering an area on the sample of about 1.32 x 0.55 mm, the magnification was 8X on the gratings. Normalized Raman spectra from eight selected lenslet regions are shown (left). The resolving power per lenslet is 450, which corresponds to a spectral resolution of 41.7 cm^{-1}, which matches the measured resolution of 42 cm^{-1}. The grating image is magnified 1.17X on the CCD, so each lenslet image has a diameter of 65 pixels, thus allowing 65/2 spectral elements to be measured, giving a theoretical spectral range of 1,365 cm^{-1}. The observed one-lenslet spectral range, ~1,250 cm^{-1}, is consistent with this value.

If there were no overlap between the Raman signals collected by the lenslets of the array for the bilayer sample used here, we would expect the Raman spectra to change rapidly for lenslets on either side of the sample interface, showing only nitrate (1062 cm^{-1}) on one side and only perchlorate (941 cm^{-1}) on the other side.[28] So, a plot of the intensity ratio of these two bands would show an abrupt change at the interface. Instead, what we see is a more gradual intensity ratio change, due to diffuse scattering in the sample, as shown in Fig. 4.7 (lower right). The intensity ratio is shown in this plot, because the Raman intensity changes a lot from lenslet to lenslet and this was not corrected. The shape of the intensity ratio curves in Fig. 4.7, are consistent with plots of Raman signal intensity versus relative offset position for spatially offset Raman.[29] In fact, the MLA-SHRS hyperspectral imaging system described here would seem to be ideal for quickly making measurements that can be used to test models of spatially offset and transmission Raman.

Figure 4.8 shows a Raman image made up of 546 lenslets (top left) for a diamond/potassium perchlorate sample, with each lenslet showing clear interference fringes. To acquire this image, the MLA was magnified by 4X onto the 150 lp/mm gratings. The 546 lenslets shown correspond to an area on the sample of 2.31 x 2.86 mm^2.

A complementary metal-oxide semiconductor (CMOS) detector (AgenaAstroproducts, QHY183M) with 2.4 micron pixels and overall chip size of 13 x 8 mm^2 was used to acquire this image. The cross section (bottom) for a selected row of lenslets shows high contrast fringes for each lenslet. Raman spectra, recovered by taking the Fourier transform of the cross section for two individual lenslets are shown (top right), for lenslets that image diamond and perchlorate regions of the sample. The size of the image of each lenslet on the gratings is 0.4 mm. For the 150 lp/mm gratings, this corresponds to a theoretical resolving power of 120, which gives a theoretical spectral resolution of 148 cm^{-1}. The measured resolution of the spectra shown in Fig. 8 are consistent with this value, at 148 cm^{-1}. This low spectral resolution is limited by the grating groove density and the total number of pixels available on the detector.

4.5 IMAGING LIMITATIONS OF THE MLA-SHRS

For the MLA-SHRS technique, the number of spatial elements that can be imaged simultaneously is determined by the grating size and the desired spectral resolution, and also depends on the laser wavelength. For an individual lenslet, the resolution is determined primarily by the number of grating grooves that are illuminated by that lenslet. Table 4.1 shows the theoretical maximum number of spatial elements that can be imaged using a 25 mm SHRS, for three different laser wavelengths and grating groove densities, assuming a spectral resolution of 20 cm^{-1}. The calculations show that using 785 nm or 532 nm laser wavelength, over ten thousand spatial points can be simultaneously imaged, with a spectral range that is limited only by the number of pixels available on the detector. Even at 244 nm, almost four thousand lenslets can theoretically be measured. Furthermore, if 30 cm^{-1} spectral resolution is permissible, then ~23,000 lenslets could be imaged at the longer

wavelengths. These calculations do not consider loss of coherence across the SHRS grating face. Loss of coherence will limit the contribution of lenslets far from the center of the grating in the horizontal direction. The extent of this depends on the coherence length of the bands being measured and the grating angle. In situations where loss of coherence might occur, a compound or curved grating could be designed to eliminate the problem.

4.6 CONCLUSIONS

A new hyperspectral Raman imaging technique is demonstrated using a spatial heterodyne Raman spectrometer with a microlens array, where the entire hypercube of spatial and spectral information is obtained in a single measurement. Raman images for a variety of sample types are demonstrated where Raman spectra, at spectral ranges from 1200 cm^{-1} to 2800 cm^{-1}, were acquired for 60 to >500 unique spatial points dependent on the type of detector used. The spectral resolution of the Raman spectra acquired for each spatial point in the images varied from 32 cm^{-1} to 148 cm^{-1}, dependent on the grating and system magnification. Calculations show that this technique can be extended to include more than 10,000 spatial points with a spectral resolution of 20 cm^{-1}, with a large spectral range.

4.7 CONFLICT OF INTEREST

The authors report there are no conflicts of interest.

4.8 ACKNOWLEDGEMENTS

We would like to thank the National Science Foundation [grant numbers CHE-1308211 and OCE-1829333] and NASA [grant numbers NNX14AI34G and 80NSSC19K1024] for funding this work.

4.9 REFERENCES

1. J. M. Harlander, F. L. Roesler, C. R. Englert, J. G. Cardon, R. R. Conway, C. M. Brown, J. Wimperis. "Robust monolithic ultraviolet interferometer for the SHIMMER instrument on STPSat-1". Appl. Opt. 2003. 42: 2829-2834.
2. A. Allen and S. M. Angel. “Miniature spatial heterodyne spectrometer for remote laser induced breakdown and Raman spectroscopy using Fresnel collection optics”. Spectrochim Acta B. 2018. 149: 91-98.
3. P. J. Treado, I. W. Levin, E. N. Lewis. “Near-infrared acousto-optic filtered spectroscopic microscopy: a solid state approach to chemical imaging”. Appl. Spec. 1992. 46(4): 553-559.
4. M. Delhaye and P. Dhamelincourt. “Raman microprobe and microscope with laser excitation”. J. Raman Spectrosc. 1975. 3: 33-34.
5. C. Brenen and I. Hunter. “Chemical imaging with a confocal scanning Fourier transform Raman microscope”. Appl. Opt. 1994. 33: 7520-7528.
6. M. Bowden, D. Gardiner, G. Rice, D. Gerrand. “Line-scanned micro Raman spectroscopy using a cooled CCD imaging detector”. J. Raman Spectrosc. 1990. 21: 37-41.
7. D. N. Batchelder, C. Cheng, W. G. D. Pitt. “Molecular imaging by Raman microscopy”. J. Adv. Mater. 1991. 3(11): 566-568.
8. G. Puppels, M. Grond, J. Greve. “Direct imaging Raman microscope based on tunable wavelength excitation and narrow-band emission detection”. Appl. Spectrosc. 1993. 47: 1256-1267.

9. P. Treado, I. Levin, E. Lewis. “High-fidelity Raman imaging spectrometry: a rapid method using an acousto-optic tunable filter”. Appl. Spectrosc. 1992. 46: 1211-1216.
10. H. Skinner, T. Cooney, S. Sharma, and S. M. Angel. “Remote Raman microimaging using an AOTF and a spatially coherent microfiber optical probe”. Appl. Spectrosc. 1996. 50: 1007-1014.
11. H. Morris, C. Hoyt, P. Miller, P. Treado. “Liquid crystal tunable filter Raman chemical imaging”. Appl. Spectrosc. 1996. 50: 805-811.
12. S. Saeed and P. Bos. “Multispectrum, spatially addressable polarization interference filter”. J. Opt. Soc. Am. A. 2002. 19: 2301-2312.
13. J. Evans. “The birefringent filter”. J. Opt. Soc. Am. 1949. 39: 229-237.
14. S. Stewart, R. J. Priore, M. P. Nelson and P. J. Treado. “Raman Imaging”. Annu. Rev. Anal. Chem. 2012. 5: 337-360.
15. K. Christensen, N. Bradley, M. Morris, R. Morrison. “Raman imaging using a tunable dual-stage liquid crystal Fabry-Perot interferometer”. Appl. Spectrosc. 49: 1120-1125.
16. J. Ma and D. Ben-Amotz. “Rapid micro-Raman imaging using fiber-bundle image compression”. Appl Spectrosc. 1997. 51: 1845-1848.
17. J. G. Dwight and T. S. Tkaczyk. “Lenslet array tunable snapshot imaging spectrometer (LATIS) for hyperspectral fluorescence microscopy”. Biomed. Opt. Express. 2017. 8(3): 1950-1964.
18. H. J. Tiziani and H. M. Uhde. “Three-dimensional analysis by a microlens-array confocal arrangement”. Appl. Opt. 1994. 33(4): 567-572.
19. H. J. Tiziani, R. Achi, R. N. Kramer and L. Wiegers. “Theoretical analysis using confocal microscopy with microlenses”. Appl. Opt. 1996. 35(1): 120-125.

20. N. R. Gomer, C. M. Gordon, P. Lucey, S. K. Sharma, J. C. Carter, S. M. Angel. “Raman Spectroscopy Using a Spatial Heterodyne Spectrometer: Proof of Concept”. Appl. Spectrosc. 2011. 65(8): 849–857.
21. N. Lamsal, S. K. Sharma, T. E. Acosta, S. M. Angel. “Stand-off UV and Visible Raman Measurements Using a Gated Spatial Heterodyne Raman Spectrometer”. Appl. Spectrosc. 2016. 70(4): 666-675.
22. J. M. Harlander. Spatial Heterodyne Spectroscopy: Interferometric Performance at Any Wavelength without Scanning. [Ph.D. Dissertation]. Madison, Wisconsin: University of Wisconsin-Madison, 1991.
23. Holospec Imaging Spectrograph instruction manual. Kaiser Optical Systems, Inc. accessed Sept 9 2019. https://psfcsv10.psfc.mit.edu/~rowan/page4/page6/assets/HoloSpec_V2.pdf
24. R. L. Aggarwal, L. W. Farrar, S. K. Saikin, X. Andrade, A. Aspuru-Guzik, D. L. Polla. “Measurement of the absolute Raman cross section of the optical phonons in type Ia natural diamond”. Solid State Commun. 2012. 152: 204-209.
25. T. E. Acosta-Maeda, A. K. Misra, J. N. Porter, D. E. Bates, S. K. Sharma. “Remote Raman Efficiencies and Cross-Sections of Organic and Inorganic Chemicals”. Appl. Spectrosc. 2017. 71(5): 1025-1038.
26. S. A. Solin and A. K. Ramdas. “Raman spectrum of diamond”. Phys. Rev. B. 1970. 1: 1687-1698.
27. N. Krishnamurthy. “Raman spectrum of crystalline potassium perchlorate”. Proc. Indian Acad. Sci. 1965. 61: 118.

28. D.L. Rousseau and R. E. Miller. “Raman spectrum of crystalline sodium nitrate”. J. Chem. Phys. 1968. 48: 3409-3413.

29. P. Matousek, I. P. Clark, E. R. Draper, M. D. Morris, A. E. Goodship, N. Everall, M. Towrie, W. F. Finney, A. W. Parker. “Subsurface Probing in Diffusely Scattering Media Using Spatially Offset Raman Spectroscopy”. Appl. Spectrosc. 2005. 59(4): 393-400.

Table 4.1: The performance characteristics for a MLA-SHRS for system that has 20 cm^{-1} resolution for one-lenslet spectra. *25 mm grating width. **23,095 lenslets at 30 cm^{-1} spectral resolution.

Wavelength (nm)	**Grating line density (lp/mm)**	**Grooves illuminated per lenslet for 20 cm^{-1} spectral resolution**	**Imaged lenslet diameter (μm)**	**Number of lenslets, horizontal direction***	**Total lenslets imaged**
785	1200	293	244	103	10,609
532	1800	444	247	101	10,201**
244	2400	999	416	60	3,600

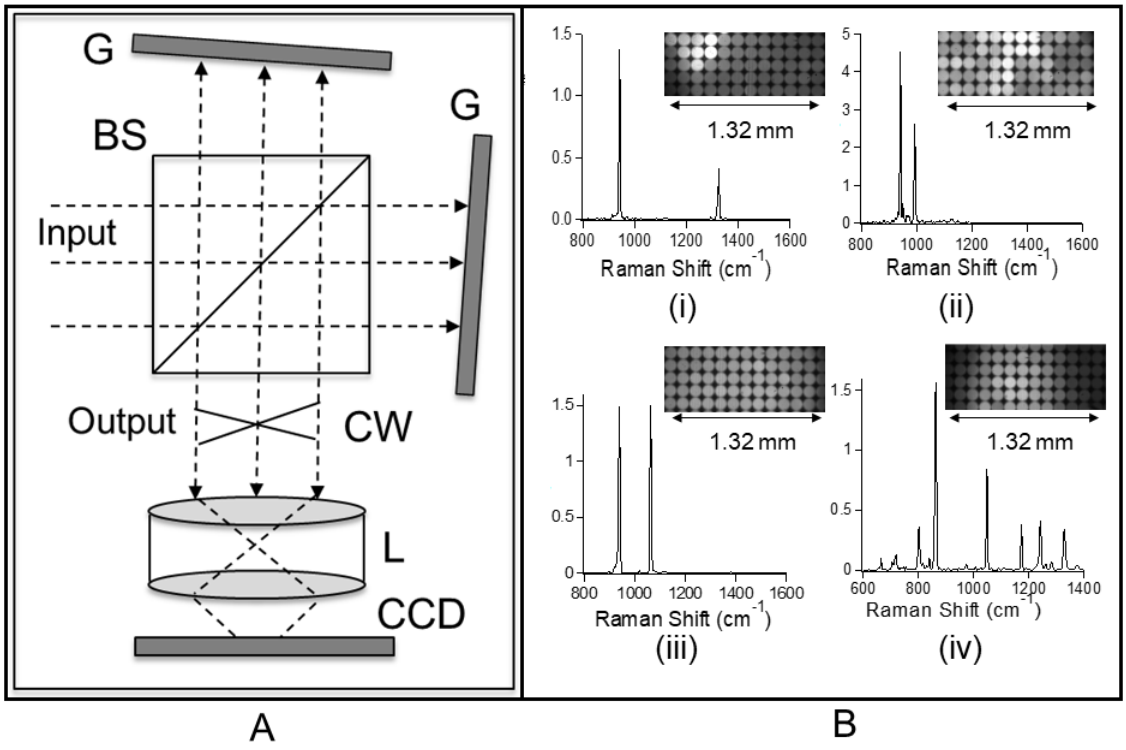

Figure 4.1 (A) Spatial heterodyne spectrometer (SHS). BS=beam splitter, G=diffraction grating, CW=crossing wavefronts, L=lens, CCD= charge coupled device detector. (B) Raman spectra measured by a SHS spectrometer for I. a diamond in potassium perchlorate pellet, II. a sodium sulfate/potassium perchlorate bilyer pellet, III. a sodium nitrate/potassium perchlorate bilyer pellet and IV. an acetaminophen/ammonium nitrate bilayer pellet. Spectra shown are the result of Fourier transforming all lenslets on the CCD. One-lenslet spectra for samples (i)-(iii) are shown in figures 5 through 7. 150 mW CW 532 nm, (i) and (ii) 10 minute acquisition, (iii) and (iv) 3 minute acquisition.

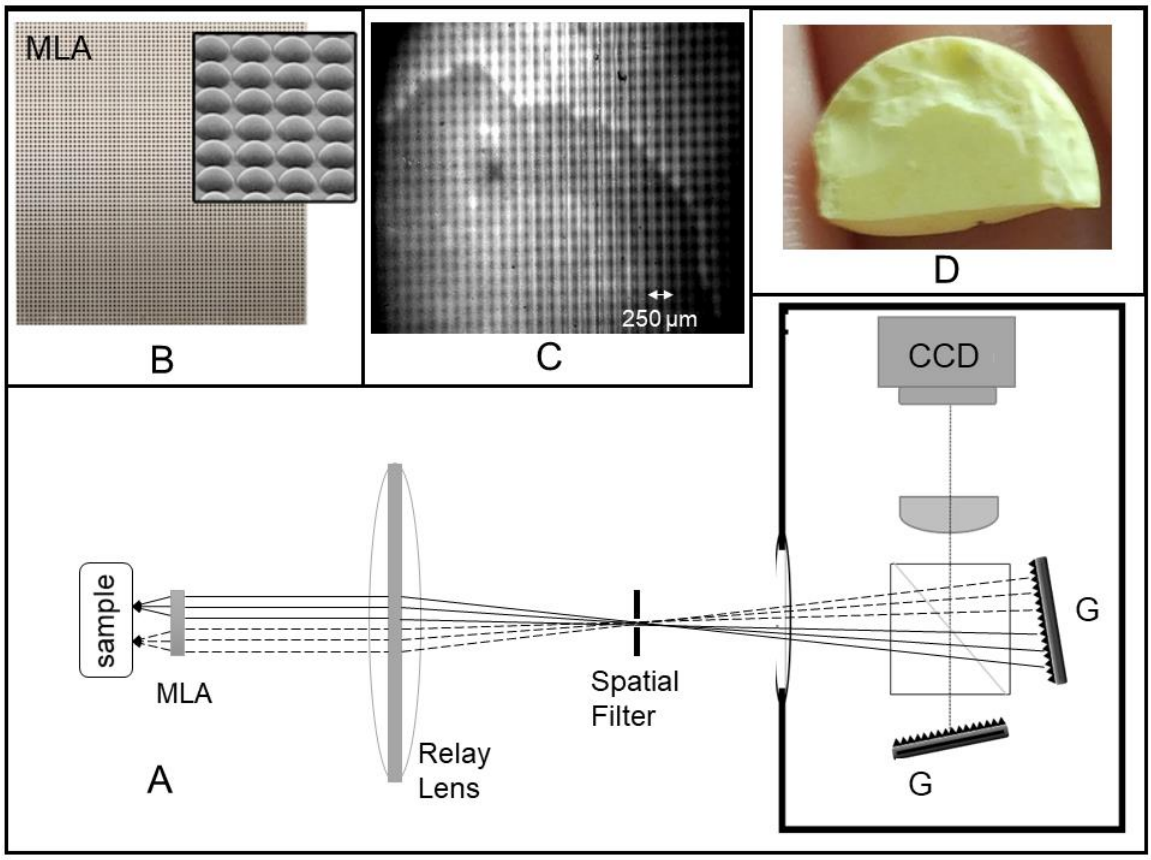

Figure 4.2 (A) Schematic of the optical path of the MLA-SHRS. G=diffraction grating and CCD= charge coupled device detector. (B) A Microlens Array illustration. A Raman image (C) for a sulfur pellet (D) measured with the MLA-SHRS showing almost all 1600 MLA lenslets being used.

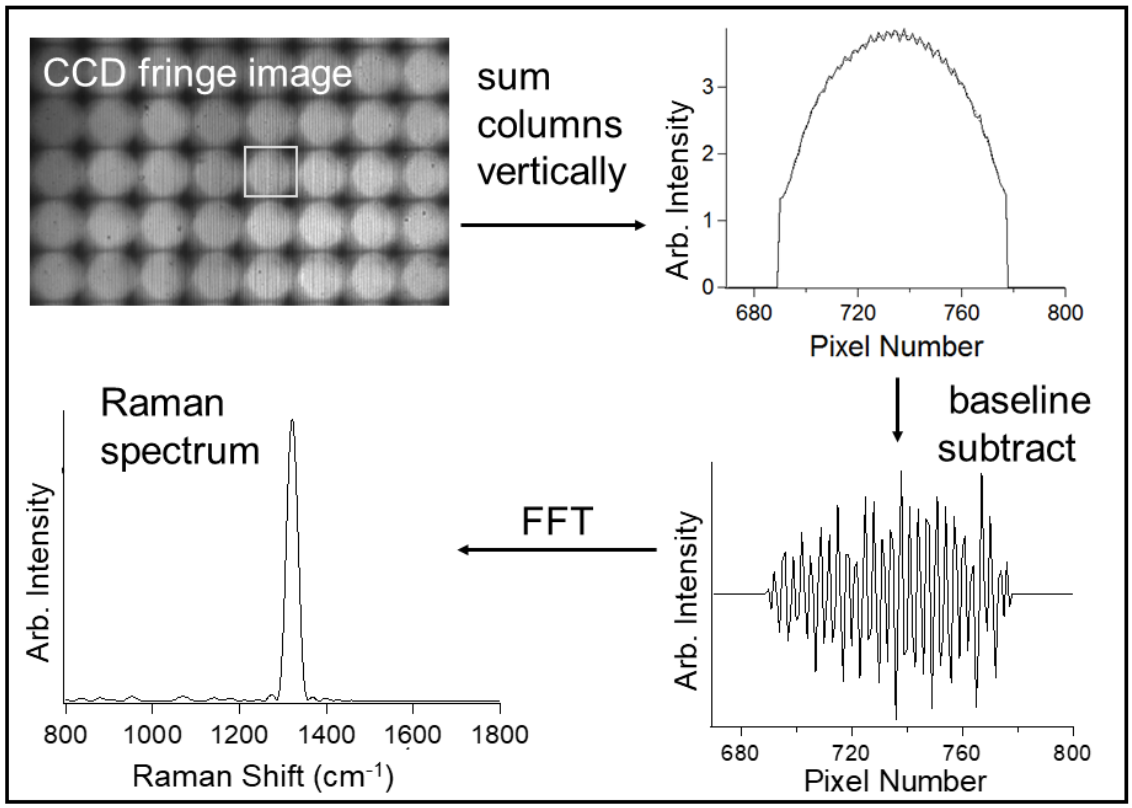

Figure 4.3 How to recover one-lenslet spectra using the MLA-SHRS. The signal is collected and measured as a fringe image on the detector (upper left). The one lenslet region of interest, shown in white, is chosen and the columns are summed to provide an interferogram superimposed on a background signal (upper right). The interferogram (lower right) is obtained by subtracting a polynomial fit, and the spectrum (lower left) is obtained by taking the one-dimensional Fourier transform of the interferogram. The sample for the spectrum shown is diamond.

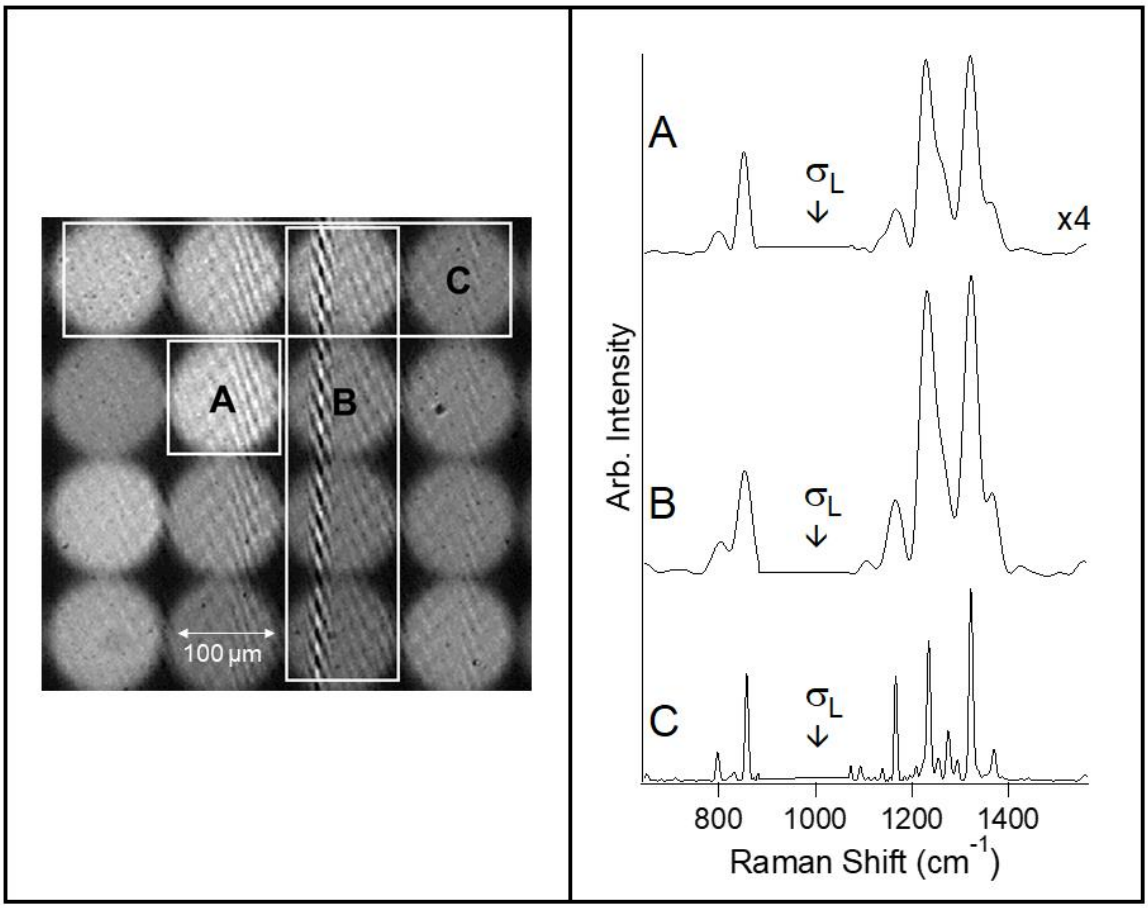

Figure 4.4 Left: The Raman image of an acetaminophen pellet measured using our MLA-SHRS in 2D-SHS configuration. The interferogram image is labeled with A, a one lenslet region of interest, B, a column of four lenslets and C, a row of four lenslets. Right: the spectra for each region of interest are shown. Littrow wavenumber is around 1000 cm^{-1}, as indicated by σ_L.

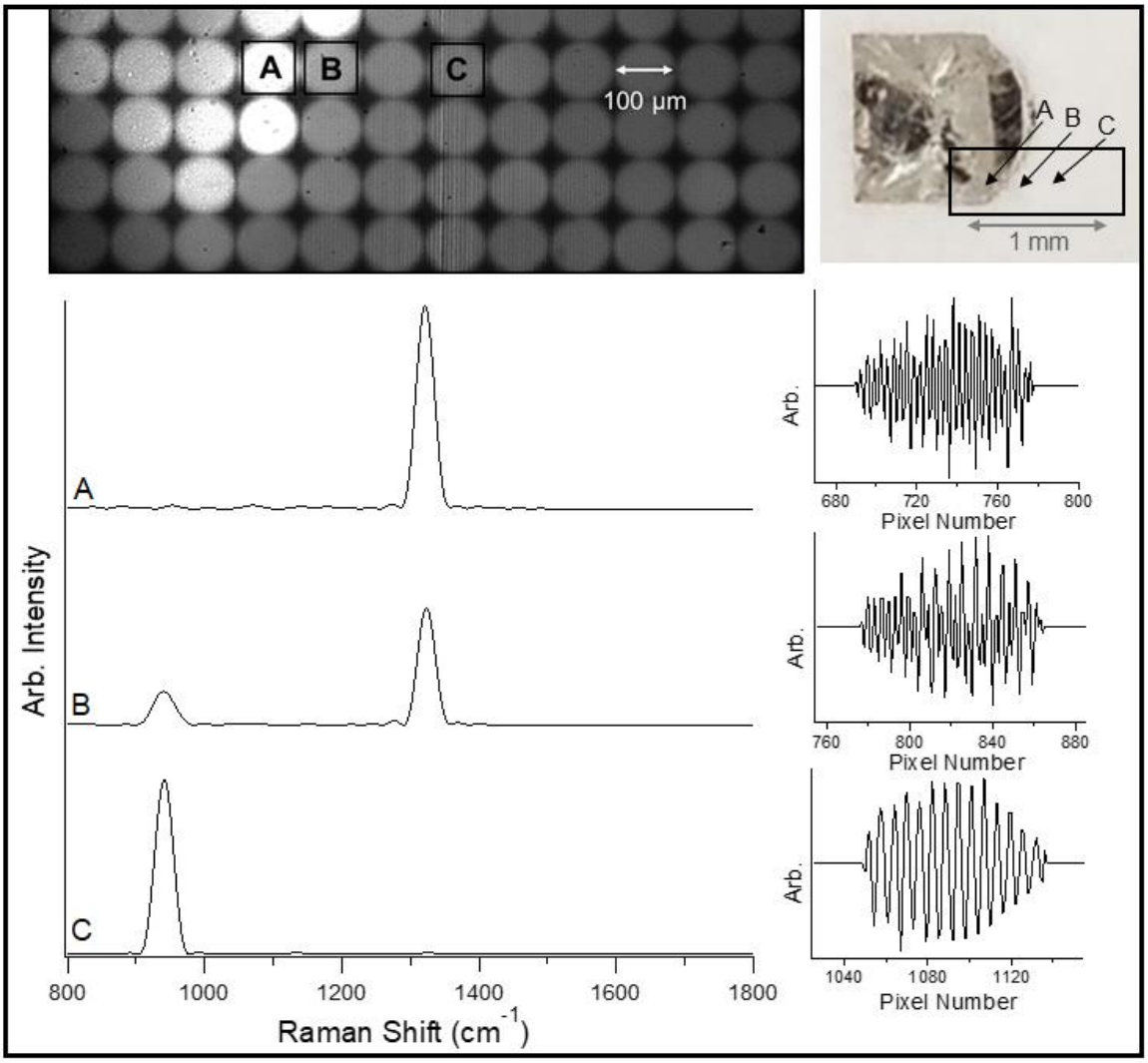

Figure 4.5 Diamond in perchlorate measured with the MLA-SHRS. Top left: the Raman image labeled with the one-lenslet regions of interest. Top right: picture of the sample with black box labeling the area measured. Bottom left: spectra corresponding to each one lenslet region of interest, offset for clarity. Bottom right: the corrected interferograms for each region of interest.

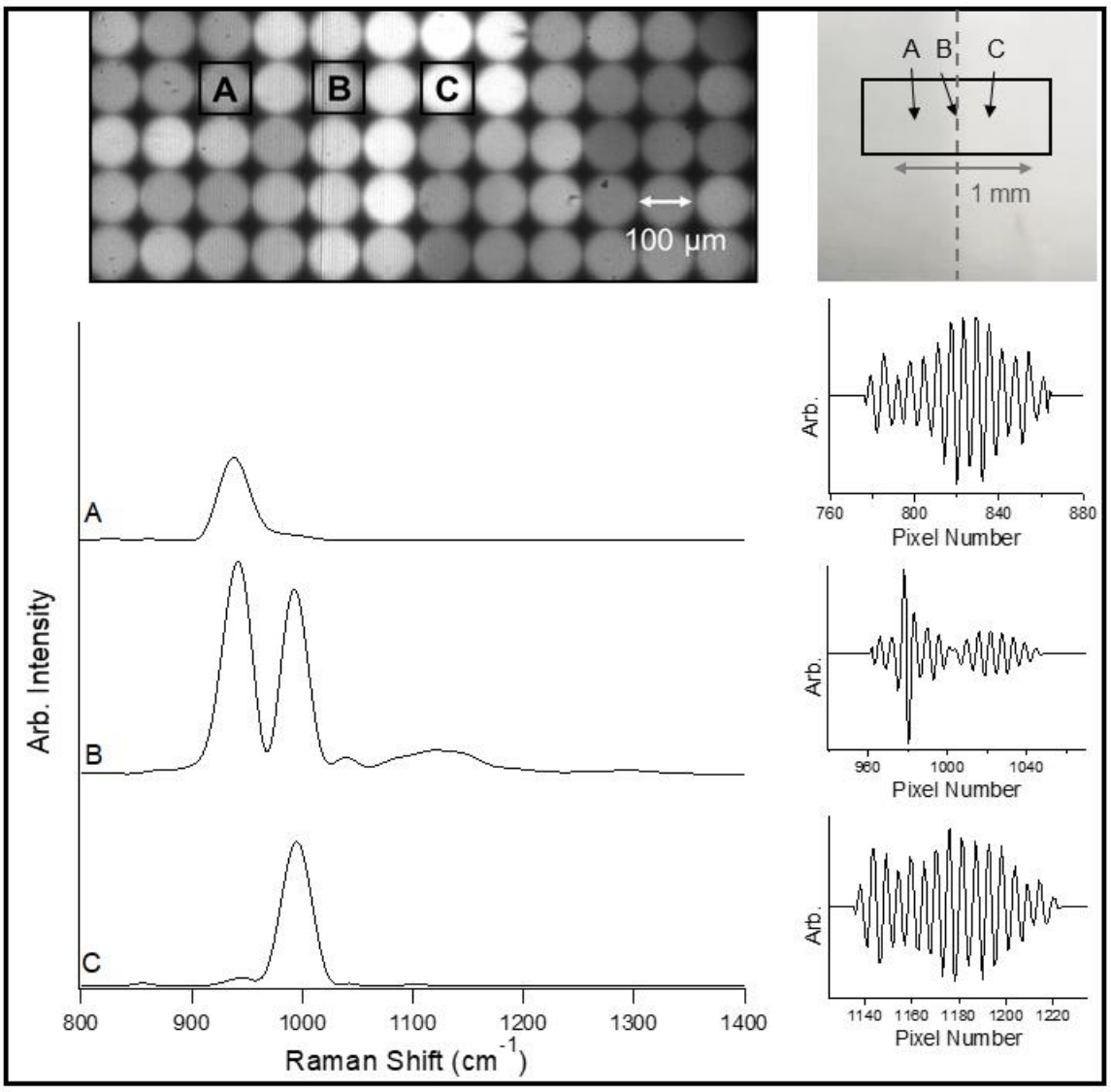

Figure 4.6 A sodium sulfate/potassium chlorate bilayer pellet measured with the MLA-SHRS. Top left: the Raman image labeled with the one-lenslet regions of interest. Top right: picture of the sample with black box indicating the area measured and grey dashed line to indicate the interface on the sample. Bottom left: spectra corresponding to each one lenslet region of interest, offset for clarity. Bottom right: the corrected interferograms for each region of interest.

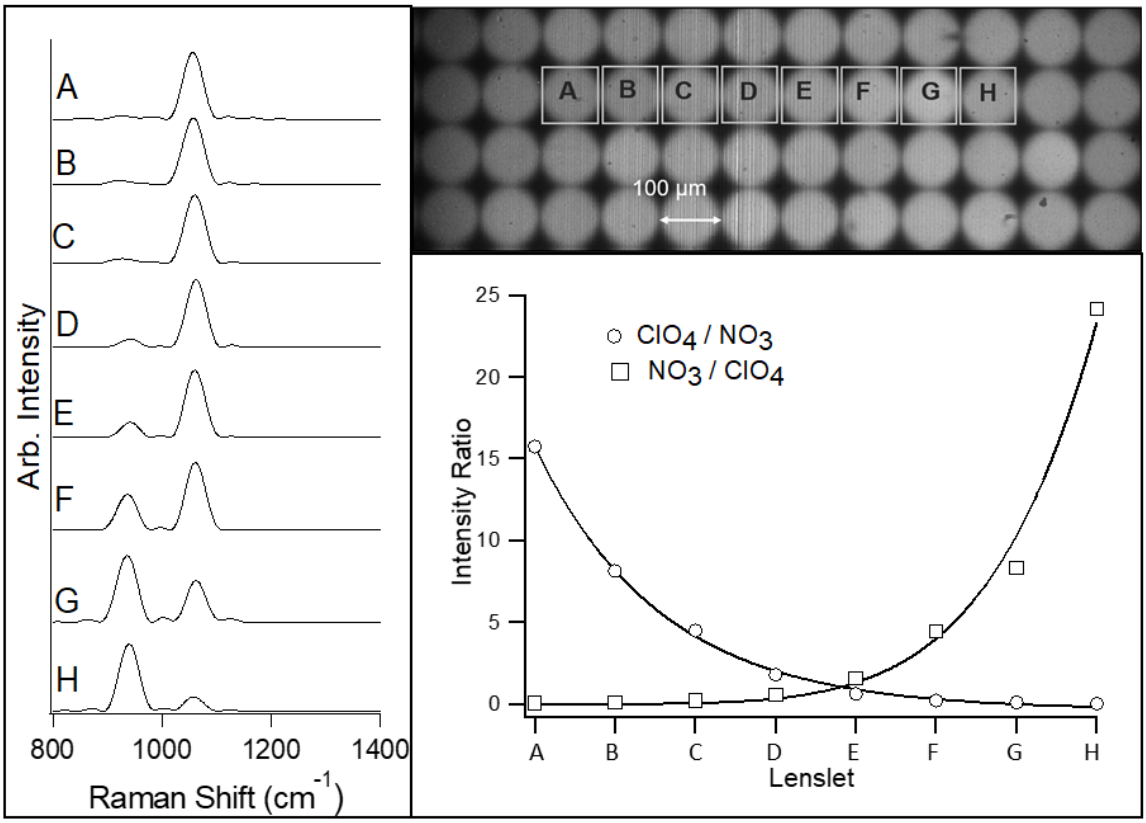

Figure 4.7 A sodium nitrate/potassium perchlorate bilayer pellet measured with the MLA-SHRS. Top right: the Raman image labeled with one-lenslet regions of interest. Left: normalized spectra corresponding to each one-lenslet region of interest, offset for clarity. Bottom right: Intensity ratios of the $KClO_4$ and $NaNO_3$ bands plotted vs lenslet location.

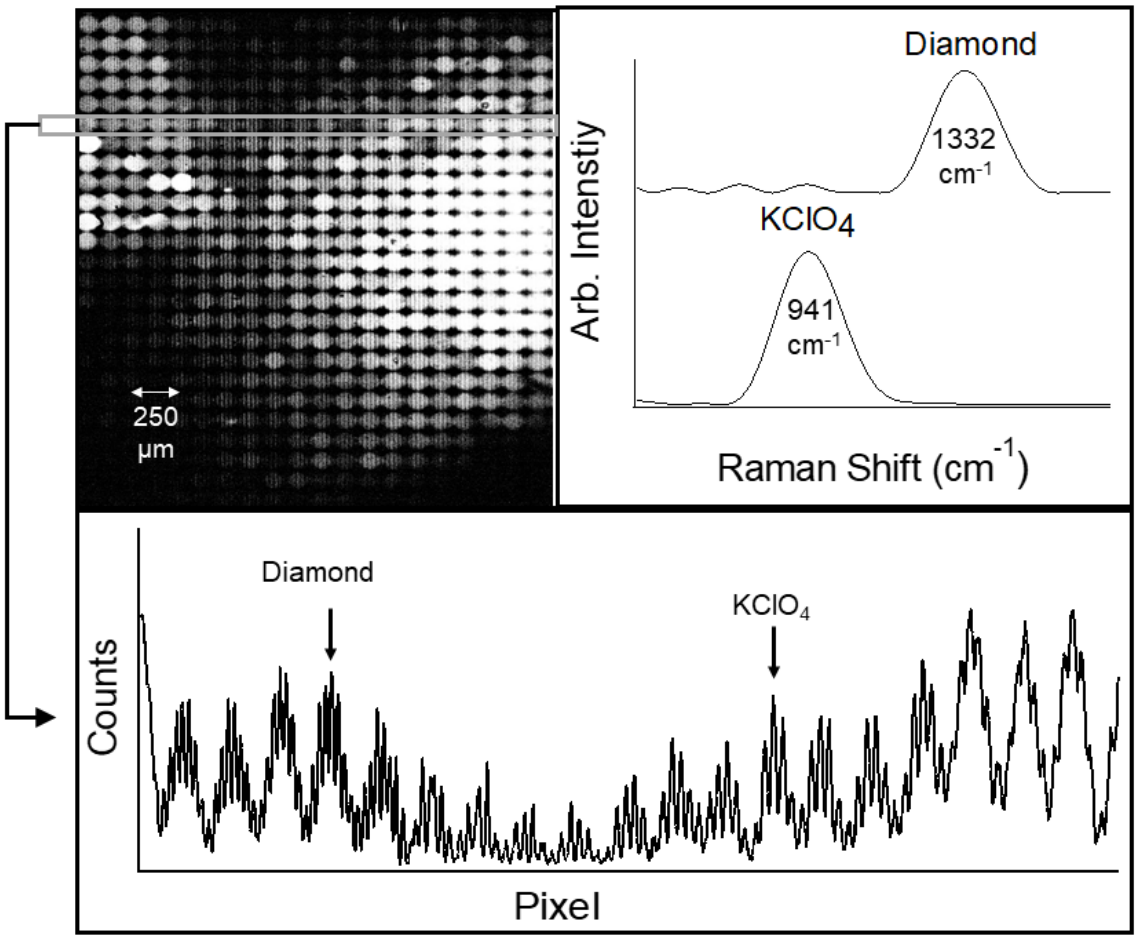

Figure 4.8 Top left: the Raman image of diamond in perchlorate, measured with MLA magnified 4X onto the SHRS gratings. Bottom: the cross section for the row of lenslets outlined in gray on the Raman image. Top right: Raman spectra corresponding to two different lenslets.

CHAPTER 5

CONCLUSIONS AND FUTURE WORK

5.1 SUMMARY AND CONCLUSIONS

NASA's 2013 Planetary Decadal Survey recommends a high priority be placed on remote sensing technology with a focus on developing and maturing novel, crosscutting, low mass/power sensors integrated into robust, low-cost system architectures. Ultraviolet/visible/infrared/Raman spectroscopes are one of the most commonly cited improvements required in instrumentation for future planned NASA missions. Improvements are needed in the four following areas: (1) Increased Resolution, (2) Reduction of Mass, (3) Radiation Resistance and (4) Ability to Operate in Extreme environments. This thesis focused on developing instrumentation for two different optical techniques, laser-induced breakdown spectroscopy (LIBS) and Raman spectroscopy, with a emphasis on addressing the needs for future space exploration.

LIBS and Raman are somewhat complementary techniques in that they both acquire information about the chemical makeup of a sample without physical contact with it. LIBS measures elemental makeup while Raman provides information about the molecular composition of the sample. LIBS has been well developed for many applications including deep ocean and space exploration. Raman is not quite as well developed as LIBS, but with advancements in photodetectors and optics this technique is rapidly becoming more applicable for real-world measurements. Raman chemical imaging is useful for analyzing heterogeneous samples because it maps Raman spectra at many different spatial locations on the sample.

The spectrometer described in this thesis, the SHS, is a wide-field, high resolution Fourier transform interferometer with no moving parts and no entrance slit. It provides 100-200 times higher light throughput than a dispersive spectrometer of comparable

resolution, and spectral resolution is not strongly dependent upon entrance aperture size. It can be tuned to any wavelength and can be built monolithically with potential for miniaturization. These qualities make it an interesting device with significant potential for space applications.

In chapter 3, a combined remote LIBS and Raman spatial heterodyne spectrometer is used to make measurements of a variety of samples at a distance of 10 m, using a ~100-mm diameter Fresnel lens as the collection optic. The results are compared to identical measurements made using a high quality ~100-mm aperture Questar long-range microscope. The overall quality of the spectra as indicated by fringe visibility in the interferograms is the same using each lens. However, spectral intensities are reduced by about a factor of 4 for the Fresnel lens, likely due to scattering and reflection losses as well as aberrations in the Fresnel optic. The results are encouraging, suggesting that Fresnel optics might be useful in applications where size and weight is restricted, such as in instruments designed for spacecraft and planetary landers.

In chapter 4, a new hyperspectral Raman imaging technique is demonstrated using a spatial heterodyne Raman spectrometer with a microlens array, where the entire hypercube of spatial and spectral information is obtained in a single measurement. Raman images for a variety of sample types are demonstrated where Raman spectra, at spectral ranges from 1200 cm^{-1} to 2800 cm^{-1}, were acquired for 60 to >500 unique spatial points dependent on the type of detector used. The spectral resolution of the Raman spectra acquired for each spatial point in the images varied from 32 cm^{-1} to 148 cm^{-1}, dependent on the grating and system magnification. Calculations show that this technique can be extended to include more than 10,000 spatial points with a spectral resolution of 20 cm^{-1},

with a large spectral range.

5.2 FUTURE WORK

Future development of the SHS for LIBS and Raman spectroscopy is focused on creating a system suitable for space exploration. Ideally, the system would entirely into a small architecture like that of a 1U CubeSat and would have minimal size, weight and power consumption requirements. This requires innovation of each component of the instrument. We have already demonstrated the utility of a lightweight Fresnel lens for signal collection. Our group has also demonstrated the use of a small uncooled CMOS detector for Raman detection. We are currently characterizing some of the first fully monolithic SHRS'.

The intended application and size of the instrument establish design restrictions. The SHS is the smallest component of the device and the laser source is the largest and heaviest, but the optics used in the system largely determine the footprint of a device. A problem we are addressing next is related to the fact that the imaging detector must be shielded from radiation interferences in the device. The SHRS uses a high-quality camera lens focused on the face of the gratings to image the interferogram onto a detector. This requires that the SHS, lens, and detector are placed in positions governed by the len's focal distance. If the interferogram was instead imaged onto a coherent fiber bundle, the detector could be anywhere in the device; allowing more design freedom for placing the detector in a radiation shielded area.

APPENDIX A

PERMISSION TO REPRINT CHAPTER 3